PHYSICAL REVIEW B **94**, 155401 (2016)

Boundary conditions at closed edge of bilayer graphene and energy bands of collapsed nanotubes

Takeshi Nakanishi[1,*] and Tsuneya Ando[2]

[1] *Research Center for Computational Design of Advanced Functional Materials, AIST, 1-1-1 Umezono, Tsukuba 305-8568, Japan*
[2] *Department of Physics, Tokyo Institute of Technology, 2-12-1 Ookayama, Meguro-ku, Tokyo 152-8551, Japan*

(Received 29 May 2016; revised manuscript received 5 September 2016; published 3 October 2016)

Band structure is systematically studied in an effective-mass scheme in collapsed armchair and zigzag nanotubes based on the model in which collapsed tubes are regarded as bilayer ribbons with closed edges. Boundary conditions at closed edges, describing the connection of the envelope wave functions between the bottom and top layers, are derived. Among electronic states in bilayers, which change sensitively depending on the relative displacement of two layers, those having wave functions matching well with the obtained boundary conditions, i.e., unaffected by the presence of closed edges, constitute important states near the Fermi level in collapsed nanotubes.

DOI: 10.1103/PhysRevB.94.155401

I. INTRODUCTION

A carbon nanotube is a cylindrically rolled-up graphene sheet [1–4], which has been studied from viewpoints of fundamental physics and applications. In a single-wall nanotube, electronic states are known to change from metallic to semiconducting depending on its circumferential vector, as predicted first by means of tight-binding models [5–14] and also by an effective-mass scheme [15–17]. When a nanotube has a large diameter, it has an additional stable structure called collapsed nanotube. This has been shown both experimentally [18–32] and theoretically [33–53]. A collapsed nanotube can be regarded as a bilayer-graphene ribbon with closed edges. The purpose of this work is to derive boundary conditions at a closed edge of a bilayer graphene and to discuss their roles in determining the band structure of collapsed nanotubes.

The band structure of various collapsed nanotubes was previously studied within an effective-mass scheme [54]. Calculated results show small and almost negligible effects of interlayer interaction in chiral nanotubes except in the close vicinity of nonchiral tubes such as armchair and zigzag. This weak interlayer interaction in chiral nanotubes is a result of the fact that interlayer hopping becomes negligibly small due to cancellation caused by rapid and quasiperiodic variation of its phase except in some special cases [55–60]. It is also related to some of epitaxially fabricated graphenes in which each layer is known to behave almost as a monolayer [61–71]. Further, the electronic structure of twisted bilayer graphene with nearly incommensurate lattice structure, both theoretically calculated [66,72–82] and experimentally observed [67,83–87], shows a linear band dispersion near zero energy, suggesting weak interlayer interaction.

On the other hand, the band structure is strongly affected by interlayer interactions in zigzag and armchair nanotubes, where cancellation does not take place. In these nonchiral nanotubes it varies depending on the relative displacement of two layers in the flattened region [54], although calculations were limited to only a few cases. Here, we perform a systematic study for these nonchiral nanotubes, regarding them as bilayer ribbons with closed edges, instead of introducing interlayer interaction starting with a cylindrical nanotube as in the previous work [54]. This ribbon model is ideal for revealing the origin of characteristic features of electronic states in these collapsed nanotubes. In fact, among energy bands of bilayer graphenes, which drastically change as a function of relative displacement of two graphene layers, those that remain unaffected by the presence of closed edges, i.e., by boundary conditions, are shown to constitute important states near the Fermi level.

This paper is organized as follows: In Sec. II, an effective-mass scheme is introduced based on a nearest-neighbor tight-binding model. In Sec. III, boundary conditions at closed edges are derived. In Sec. IV, the band structure of displaced bilayer graphenes is discussed. In Sec. V, some examples of energy bands of collapsed nanotubes are presented with emphasis on relation to special features of reflection coefficients at closed edges, to be discussed in Appendix B. In Sec. VI, discussion and a short summary are given. In Appendix A, symmetry of the effective potentials under time-reversal operation is discussed. In Appendix B, the reflection coefficients at closed edges and associated quantization into energy bands are analytically investigated for some representative examples.

II. EFFECTIVE-MASS DESCRIPTION

We consider collapsed armchair and zigzag nanotubes. Figure 1 shows schematic illustration of a cross section of a collapsed tube with circumference L. In the central region with width $\sim L_F/2$ the tube is flattened, forming a displaced bilayer graphene with bottom and top layers, denoted by 1 and 2, respectively. The right-hand side of the bottom layer with width $\sim L_R$ is connected to the right edge of the top layer and the left-hand side of the bottom layer with width $\sim L_L$ is connected to the left edge of the top layer. We set $L_C = L_L + L_R$ and $L_F + L_C = L$, and shall consider the symmetric case $L_L = L_R = L_C/2$ in explicit numerical calculations presented below.

Before collapsing, each single-wall nanotube is specified by chiral vector $\boldsymbol{L} = n_a\boldsymbol{a} + n_b\boldsymbol{b}$, where $\boldsymbol{a}$ and $\boldsymbol{b}$ are primitive

---

[*] Present address: Mathematics for Advanced Materials–Open Innovation Laboratory, AIST, c/o Advanced Institute for Materials Research, Tohoku University, 2-1-1 Katahira, Aoba, Sendai 980-8577, Japan; t.nakanishi@aist.go.jp

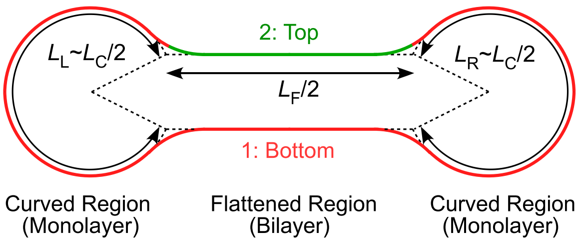

FIG. 1. A schematic illustration of cross section of a collapsed carbon nanotube. The (red) bottom and (green) top layers are denoted as 1 and 2, respectively.

translation vectors shown in Fig. 2(a), n_a and n_b are integers, $L = |\boldsymbol{L}|$, and $|\boldsymbol{a}| = |\boldsymbol{b}| = a$ with lattice constant $a = 0.246$ nm. The nanotube is metallic for $\nu = 0$ and semiconducting for $\nu = \pm 1$, where integer ν is defined by

$$n_a + n_b = 3n + \nu, \tag{1}$$

with integer n [15–17]. The angle η between $\boldsymbol{a}$ and $\boldsymbol{L}$ is called the chiral angle. An armchair nanotube has $\eta = \pi/6$ and $\boldsymbol{L} = n(2\boldsymbol{a} + \boldsymbol{b})$ or $L/(\sqrt{3}a) = n$ with integer n, and is therefore always metallic ($\nu = 0$). On the other hand, a zigzag tube has $\eta = 0$ and $\boldsymbol{L} = n\boldsymbol{a}$ or $L/a = n$, and can be metallic or semiconducting depending on n. We consider the coordinates (x,y) rotated around the origin by η such that the x axis is always along the circumference of a nanotube.

In the bottom layer of the flattened region, a unit cell contains two carbon atoms denoted by A_1 and B_1. Three vectors connecting nearest-neighbor atoms are denoted by $\boldsymbol{\tau}_1$, $\boldsymbol{\tau}_2$, and $\boldsymbol{\tau}_3$. The origin of the coordinates is chosen at a B site, i.e., a B site is given by $\boldsymbol{R}_{B1} = n_{a1}\boldsymbol{a} + n_{b1}\boldsymbol{b}$ and an A site is $\boldsymbol{R}_{A1} = n_{a1}\boldsymbol{a} + n_{b1}\boldsymbol{b} + \boldsymbol{\tau}$ with integer n_{a1} and n_{b1} and $\boldsymbol{\tau} \equiv \boldsymbol{\tau}_1 = (\boldsymbol{a} + 2\boldsymbol{b})/3$. In the coordinate system (x',y') fixed onto the graphene, we have $\boldsymbol{a} = a(1,0)$, $\boldsymbol{b} = a(1/2,\sqrt{3}/2)$, and $\boldsymbol{\tau} = a(0,1/\sqrt{3})$. The amount of the displacement of the top layer relative to the bottom layer is denoted by $\boldsymbol{\xi}$, i.e., $\boldsymbol{R}_{B2} = n_{a2}\boldsymbol{a} + n_{b2}\boldsymbol{b} + \boldsymbol{\xi}$ and $\boldsymbol{R}_{A2} = n_{a2}\boldsymbol{a} + n_{b2}\boldsymbol{b} + \boldsymbol{\tau} + \boldsymbol{\xi}$. As a function of $\xi \equiv |\boldsymbol{\xi}|$, the structure varies with period of $\sqrt{3}a$ in armchair tubes and with period of a in zigzag tubes.

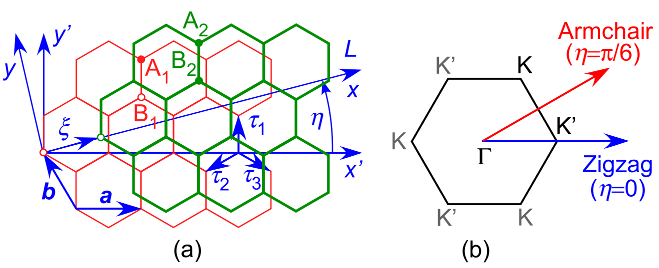

(a) (b)

FIG. 2. (a) The lattice structure and coordinate systems of a displaced bilayer graphene. On the (red) bottom layer, carbon atoms are denoted as A_1 and B_1 and on the (green) top layer as A_2 and B_2. Their relative displacement is denoted by $\boldsymbol{\xi}$. (b) The first Brillouin zone and K and K' points in monolayer graphene.

In a tight-binding model, the wave function in layer j ($j = 1,2$) is written as

$$\psi_j(\boldsymbol{r}) = \sum_{\boldsymbol{R}=\boldsymbol{R}_{Aj}} \psi_{Aj}(\boldsymbol{R})\phi(\boldsymbol{r}-\boldsymbol{R}) + \sum_{\boldsymbol{R}=\boldsymbol{R}_{Bj}} \psi_{Bj}(\boldsymbol{R})\phi(\boldsymbol{r}-\boldsymbol{R}), \tag{2}$$

where $\phi(\boldsymbol{r})$ denotes a π orbital. In the monolayer region, the amplitude ψ at atomic sites $\boldsymbol{R} = \boldsymbol{R}_{A1}$ or $\boldsymbol{R}_{B1}$ satisfies

$$\varepsilon\psi_{A1}(\boldsymbol{R}_{A1}) = -\gamma_0 \sum_l \psi_{B1}(\boldsymbol{R}_{A1} - \boldsymbol{\tau}_l), \tag{3}$$

$$\varepsilon\psi_{B1}(\boldsymbol{R}_{B1}) = -\gamma_0 \sum_l \psi_{A1}(\boldsymbol{B}_{B1} + \boldsymbol{\tau}_l), \tag{4}$$

where γ_0 is the hopping integral between nearest-neighbor atoms ($\gamma_0 \sim 3$ eV). In the bilayer region, the same equation is satisfied by $\psi_{A2}(\boldsymbol{R}_{A2})$ and $\psi_{B2}(\boldsymbol{R}_{B2})$ except that interlayer hopping $V(\boldsymbol{R},\boldsymbol{R}')$ is included, where $V(\boldsymbol{R},\boldsymbol{R}')$ is nonzero only when carbon atoms at sites $\boldsymbol{R}$ and $\boldsymbol{R}'$ in different layers are very closely located. Because π orbitals are symmetric within each layer, $V(\boldsymbol{R},\boldsymbol{R}')$ is a function of $|\boldsymbol{R} - \boldsymbol{R}'|$.

In the following, Hamiltonian and boundary conditions in an effective-mass scheme will be derived from this nearest-neighbor tight-binding model and exclusively used for actual calculations of the band structure. This scheme itself is not limited to tight-binding models, however. For states near the Fermi level in the vicinity of K and K' points with wave vectors $\boldsymbol{K} = (2\pi/a)(1/3,\,1/\sqrt{3})$ and $\boldsymbol{K}' = (2\pi/a)(2/3,\,0)$, respectively, the amplitudes are written as

$$\psi_{Aj}(\boldsymbol{R}) = e^{i\chi_j}\big[e^{i\boldsymbol{K}\cdot\boldsymbol{R}}F^K_{Aj}(\boldsymbol{R}) + e^{i\eta}e^{i\boldsymbol{K}'\cdot\boldsymbol{R}}F^{K'}_{Aj}(\boldsymbol{R})\big], \tag{5}$$

$$\psi_{Bj}(\boldsymbol{R}) = e^{i\chi_j}\big[-\omega e^{i\eta}e^{i\boldsymbol{K}\cdot\boldsymbol{R}}F^K_{Bj}(\boldsymbol{R}) + e^{i\boldsymbol{K}'\cdot\boldsymbol{R}}F^{K'}_{Bj}(\boldsymbol{R})\big], \tag{6}$$

with $\omega = \exp(2\pi i/3)$ and χ_j being an arbitrary phase to be appropriately determined later [17]. Envelope functions $F^K_{Aj}(\boldsymbol{r})$, $F^K_{Bj}(\boldsymbol{r})$, $F^{K'}_{Aj}(\boldsymbol{r})$, and $F^{K'}_{Bj}(\boldsymbol{r})$ are assumed to be slowly varying in the scale of the lattice constant. The effective-mass scheme is valid and well reproduces electronic properties as well as the band structure for energy range given by $|\varepsilon| \lesssim \gamma_0$ [15–17].

In the monolayer region, the envelope functions at the K point satisfy the Schrödinger equation [17]

$$\mathcal{H}^K_0 \boldsymbol{F}^K_1(\boldsymbol{r}) = \varepsilon \boldsymbol{F}^K_1(\boldsymbol{r}), \tag{7}$$

$$\mathcal{H}^K_0 = \gamma(\boldsymbol{\sigma}\cdot\hat{\boldsymbol{k}}), \tag{8}$$

$$\boldsymbol{F}^K_1(\boldsymbol{r}) = \begin{pmatrix} F^K_{A1}(\boldsymbol{r}) \\ F^K_{B1}(\boldsymbol{r}) \end{pmatrix}, \tag{9}$$

where $\gamma = \sqrt{3}a\gamma_0/2$ is the band parameter, $\hat{\boldsymbol{k}} = (\hat{k}_x,\hat{k}_y) = -i\nabla$ is a wave-vector operator, and $\boldsymbol{\sigma} = (\sigma_x,\sigma_y)$ and σ_z (introduced below) are the Pauli matrices. In the bilayer region,

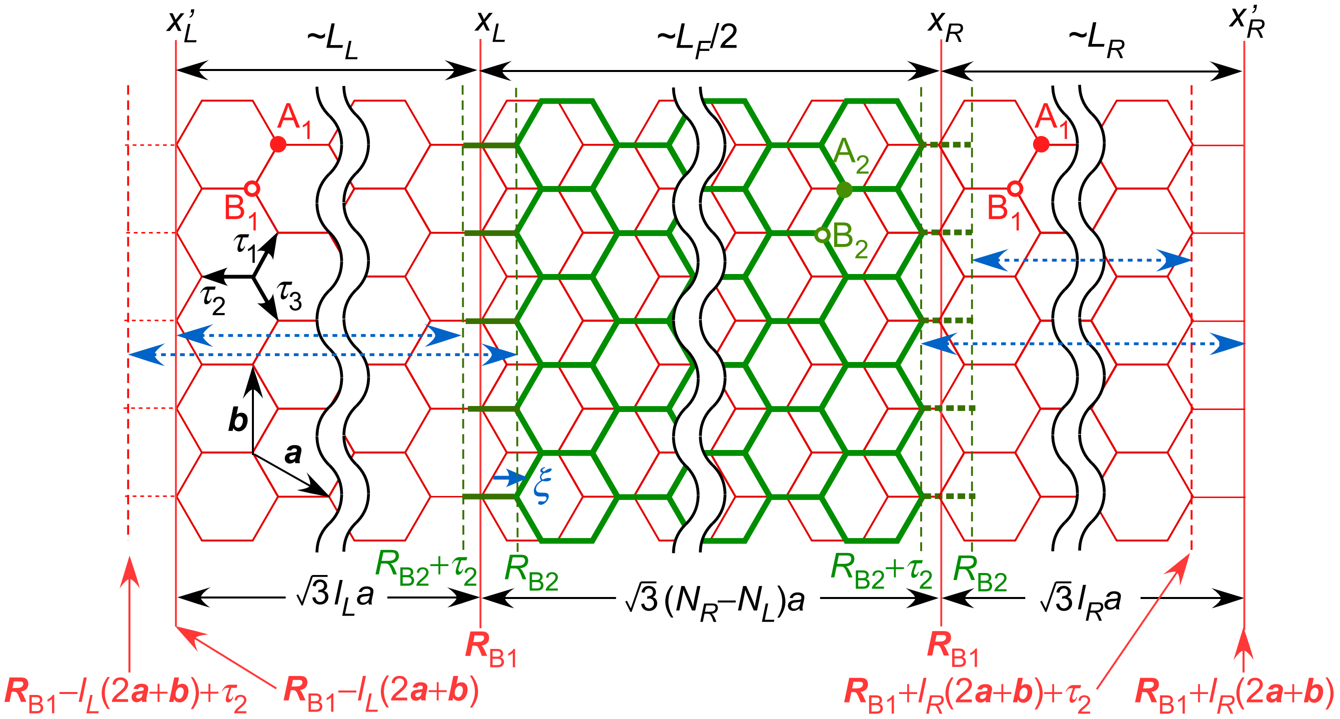

FIG. 3. A development map of a collapsed armchair nanotube. In the central region, the tube is flattened, forming a displaced bilayer graphene with width $L_F/2$ consisting of (red) bottom and (green) top layers, denoted by 1 and 2, respectively. The right-hand side of the bottom layer with width L_R is connected to the right edge of the top layer and the left-hand side of the bottom layer with width L_L is connected to the left edge of the top layer.

the Schrödinger equation becomes

$$\mathcal{H}^K \boldsymbol{F}^K(\boldsymbol{r}) = \varepsilon \boldsymbol{F}^K(\boldsymbol{r}), \tag{10}$$

$$\mathcal{H}^K = \begin{pmatrix} \mathcal{H}_0^K & V^K(\boldsymbol{\xi}) \\ V^{K\dagger}(\boldsymbol{\xi}) & \mathcal{H}_0^K \end{pmatrix}, \tag{11}$$

$$\boldsymbol{F}^K(\boldsymbol{r}) = \begin{pmatrix} \boldsymbol{F}_1^K(\boldsymbol{r}) \\ \boldsymbol{F}_2^K(\boldsymbol{r}) \end{pmatrix}, \tag{12}$$

where $V^K(\boldsymbol{\xi})$ is a (2,2) matrix representing interlayer interaction strongly dependent on the relative displacement $\boldsymbol{\xi}$. For the K' point, the time-reversal symmetry gives

$$\mathcal{H}_0^{K'} = \sigma_z \mathcal{H}_0^{K*} \sigma_z = \gamma(\boldsymbol{\sigma}^* \cdot \boldsymbol{k}), \tag{13}$$

$$V^{K'}(\boldsymbol{\xi}) = \sigma_z V^K(\boldsymbol{\xi})^* \sigma_z e^{-2i\chi_{12}} e^{i(\boldsymbol{K}+\boldsymbol{K}')\cdot\boldsymbol{\xi}}, \tag{14}$$

with

$$\chi_{12} \equiv \chi_1 - \chi_2, \tag{15}$$

as shown in Appendix A.

III. BOUNDARY CONDITIONS

A development map of a collapsed armchair tube with $\eta = \pi/6$ is shown in Fig. 3. In the left boundary region, we set $\boldsymbol{R}_{B1}$ on line $x_L = \sqrt{3}N_L a$, $\boldsymbol{R}_{B2} = \boldsymbol{R}_{B1} + \boldsymbol{\xi}$, and $L_L = \sqrt{3}a\, l_L$. Then, the connection of the bottom layer to the top layer gives

$$\psi_{B2}(\boldsymbol{R}_{B2}) = -\psi_{A1}[\boldsymbol{R}_{B1} - l_L(2\boldsymbol{a}+\boldsymbol{b}) + \boldsymbol{\tau}_2], \tag{16}$$

$$\psi_{B1}[\boldsymbol{R}_{B1} + l_L(2\boldsymbol{a}+\boldsymbol{b})] = -\psi_{A2}(\boldsymbol{R}_{B2} + \boldsymbol{\tau}_2), \tag{17}$$

where the amplitudes on the right-hand side are extrapolated from the corresponding region. The negative sign corresponds to the fact that the sign of the π orbital in the monolayer region is opposite to that on the top layer because of the cylindrical form of the closed edge. As has been previously discussed [54], these give the following conditions for the envelope functions:

$$\boldsymbol{F}_2^K(x_L) = e^{i\chi} \sigma_y \boldsymbol{F}_1^K(x'_L), \tag{18}$$

$$\boldsymbol{F}_2^{K'}(x_L) = e^{i\chi} \sigma_y \boldsymbol{F}_1^{K'}(x'_L), \tag{19}$$

with $x'_L = x_L - L_L$ and

$$\chi(\xi) = \chi_{12} - \frac{2\pi\xi}{\sqrt{3}a}, \tag{20}$$

where $\boldsymbol{\xi} = \xi(2\boldsymbol{a}+\boldsymbol{b})/(\sqrt{3}a)$.

In nanotubes, states are specified by wave vector k $(= k_y)$ along the axis direction. Then, the Schrödinger equation in the monolayer region gives

$$\boldsymbol{F}_{1k}^K(x'_L) = U^K(-L_L)\boldsymbol{F}_{1k}^K(x_L), \tag{21}$$

$$\boldsymbol{F}_{1k}^{K'}(x'_L) = U^{K'}(-L_L)\boldsymbol{F}_{1k}^{K'}(x_L), \tag{22}$$

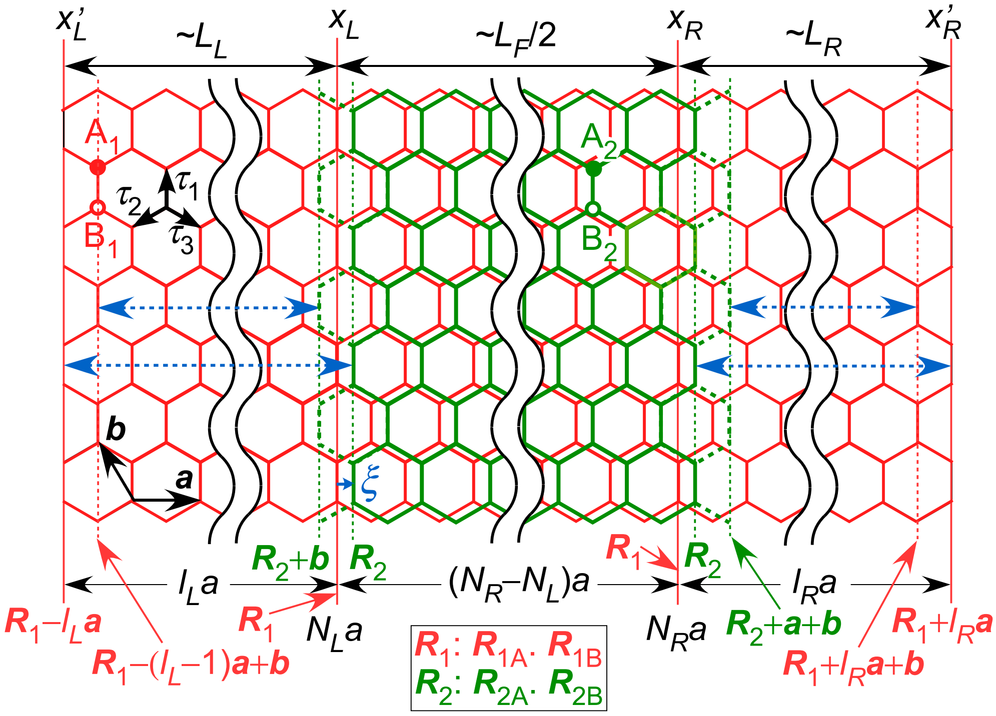

FIG. 4. A development map of a collapsed zigzag nanotube.

where $U^K(x)$ and $U^{K'}(x)$ are (2,2) transfer matrices in the monolayer region. Their explicit expressions are given in Appendix B 1. Thus, we have

$$\boldsymbol{F}_{2k}^{K}(x_L) = e^{i\chi}\sigma_y U_L^K \boldsymbol{F}_{1k}^{K}(x_L), \tag{23}$$

$$\boldsymbol{F}_{2k}^{K'}(x_L) = e^{i\chi}\sigma_y U_L^{K'} \boldsymbol{F}_{1k}^{K'}(x_L), \tag{24}$$

with $U_L^K \equiv U^K(-L_L)$ and $U_L^{K'} \equiv U^{K'}(-L_L)$.

In the right boundary region, we set $\boldsymbol{R}_{B1}$ on line $x_R = \sqrt{3}N_R a$, $\boldsymbol{R}_{B2} = \boldsymbol{R}_{B1} + \boldsymbol{\xi}$, and $L_R = \sqrt{3}a\, l_R$. The boundary conditions are given by

$$\psi_{A2}(\boldsymbol{R}_{B2} + \boldsymbol{\tau}_2) = -\psi_{B1}[\boldsymbol{R}_{B1} + l_R(2\boldsymbol{a} + \boldsymbol{b})], \tag{25}$$

$$\psi_{A1}[\boldsymbol{R}_{B1} + l_R(2\boldsymbol{a} + \boldsymbol{b}) + \boldsymbol{\tau}_2] = -\psi_{B2}(\boldsymbol{R}_{B2}), \tag{26}$$

where the amplitudes on the right-hand side are again extrapolated from the corresponding region. For the envelope functions, the conditions are written as

$$\boldsymbol{F}_2^K(x_R) = e^{i\chi}\sigma_y \boldsymbol{F}_1^K(x'_R), \tag{27}$$

$$\boldsymbol{F}_2^{K'}(x_R) = e^{i\chi}\sigma_y \boldsymbol{F}_1^{K'}(x'_R), \tag{28}$$

with $x'_R = x_R + L_R$. These give

$$\boldsymbol{F}_{2k}^{K}(x_R) = e^{i\chi}\sigma_y U_R^K \boldsymbol{F}_{1k}^{K}(x_R), \tag{29}$$

$$\boldsymbol{F}_{2k}^{K'}(x_R) = e^{i\chi}\sigma_y U_R^{K'} \boldsymbol{F}_{1k}^{K'}(x_R), \tag{30}$$

with $U_R^K \equiv U^K(L_R)$ and $U_R^{K'} \equiv U^{K'}(L_R)$.

The appearance of σ_y in the boundary conditions corresponds to the fact that the A and B sublattices are exchanged under the π rotation around an axis parallel to the y axis. Furthermore, there is no mixing between the K and K' points, corresponding to the fact that they are mapped onto different points in the one-dimensional Brillouin zone [see Fig. 2(b)].

In the bilayer region, we have

$$\begin{pmatrix} \boldsymbol{F}_{1k}^{K}(x_R) \\ \boldsymbol{F}_{2k}^{K}(x_R) \end{pmatrix} = \begin{pmatrix} U_{11}^K & U_{12}^K \\ U_{21}^K & U_{22}^K \end{pmatrix} \begin{pmatrix} \boldsymbol{F}_{1k}^{K}(x_L) \\ \boldsymbol{F}_{2k}^{K}(x_L) \end{pmatrix}, \tag{31}$$

where $U^K \equiv U^K(x_R - x_L)$ is a (4,4) transfer matrix for given $k\ (= k_y)$ and ε, which can easily be calculated once the bilayer Hamiltonian is explicitly given. Eliminating the component of the wave functions in the top layer, we have

$$\begin{pmatrix} -1 & U_{11}^K + e^{i\chi}U_{12}^K\sigma_y U_L^K \\ -e^{i\chi}\sigma_y U_R^K & U_{21}^K + e^{i\chi}U_{22}^K\sigma_y U_L^K \end{pmatrix} \begin{pmatrix} \boldsymbol{F}_{1k}^{K}(x_R) \\ \boldsymbol{F}_{1k}^{K}(x_L) \end{pmatrix} = 0. \tag{32}$$

The condition for the presence of a nontrivial solution gives the energy band of a collapsed nanotube:

$$\begin{vmatrix} -1 & U_{11}^K + e^{i\chi}U_{12}^K\sigma_y U_L^K \\ -e^{i\chi}\sigma_y U_R^K & U_{21}^K + e^{i\chi}U_{22}^K\sigma_y U_L^K \end{vmatrix} = 0. \tag{33}$$

Formally, the same expression is obtained for the K' point except that K is replaced with K'.

Next, we consider the left boundary in zigzag tubes $\eta = 0$ illustrated in Fig. 4. Let $\boldsymbol{R}_{A1}$ and $\boldsymbol{R}_{B1}$ be on line $x_L = N_L a$, $\boldsymbol{R}_{A2} = \boldsymbol{R}_{A1} + \boldsymbol{\xi}$, $\boldsymbol{R}_{B2} = \boldsymbol{R}_{B1} + \boldsymbol{\xi}$, and $L_L = l_L a$. Then, the connection of the left boundary of the monolayer region to the left edge of the top layer of the bilayer region gives

$$\psi_{A2}(\boldsymbol{R}_{A2}) = -\psi_{A1}(\boldsymbol{R}_{A1} - l_L\boldsymbol{a}), \tag{34}$$

$$\psi_{B2}(\boldsymbol{R}_{B2}) = -\psi_{B1}(\boldsymbol{R}_{B1} - l_L\boldsymbol{a}), \tag{35}$$

$$\psi_{A1}(\boldsymbol{R}_{A1} - (l_L - 1)\boldsymbol{a} + \boldsymbol{b}) = -\psi_{A2}(\boldsymbol{R}_{A2} + \boldsymbol{b}), \tag{36}$$

$$\psi_{B1}(\boldsymbol{R}_{B1} - (l_L - 1)\boldsymbol{a} + \boldsymbol{b}) = -\psi_{B2}(\boldsymbol{R}_{B2} + \boldsymbol{b}), \tag{37}$$

where the amplitudes on the right-hand side are extrapolated from the corresponding regions.

The above conditions give the following for the envelope functions:

$$\boldsymbol{F}_2^K(x_L,y) = -\omega^{+n_L} e^{i\chi'} \sigma_z \boldsymbol{F}_1^{K'}(x'_L,y), \tag{38}$$

$$\boldsymbol{F}_2^{K'}(x_L,y) = -\omega^{-n_L} e^{i\chi''} \sigma_z \boldsymbol{F}_1^{K}(x'_L,y), \tag{39}$$

with $n_L = N_L + l_L - 1$, $x'_L = x_L - l_L a$, and

$$\chi'(\xi) = \chi_{12} - \frac{2\pi\xi}{3a}, \quad \chi''(\xi) = \chi_{12} - \frac{4\pi\xi}{3a}, \tag{40}$$

where we set $\boldsymbol{\xi} = \xi\boldsymbol{a}/a$. These show that the K and K' points are exchanged with a phase dependent on the position x_L and the length of the monolayer region l_L. This behavior corresponds to the exchange of the K and K' points under the π rotation around a line parallel to the y axis [see Fig. 2(b)].

At the right boundary, we set $\boldsymbol{R}_{A1}$ and $\boldsymbol{R}_{B1}$ be on line $x_R = N_R a$, $\boldsymbol{R}_{A2} = \boldsymbol{R}_{A1} + \boldsymbol{\xi}$, $\boldsymbol{R}_{B2} = \boldsymbol{R}_{B1} + \boldsymbol{\xi}$, and $L_R = l_R\, a$. Then, the connection gives

$$\psi_{A2}(\boldsymbol{R}_{A2}) = -\psi_{A1}(\boldsymbol{R}_{A1} + l_R\boldsymbol{a}), \tag{41}$$

$$\psi_{B2}(\boldsymbol{R}_{B2}) = -\psi_{B1}(\boldsymbol{R}_{B1} + l_R\boldsymbol{a}), \tag{42}$$

$$\psi_{A1}(\boldsymbol{R}_{A1} + l_R\boldsymbol{a} + \boldsymbol{b}) = -\psi_{A2}(\boldsymbol{R}_{A2} + \boldsymbol{a} + \boldsymbol{b}), \tag{43}$$

$$\psi_{B1}(\boldsymbol{R}_{B1} + l_R\boldsymbol{a} + \boldsymbol{b}) = -\psi_{B2}(\boldsymbol{R}_{B2} + \boldsymbol{a} + \boldsymbol{b}), \tag{44}$$

and then

$$\boldsymbol{F}_2^K(x_R,y) = -\omega^{+n_R} e^{i\chi'} \sigma_z \boldsymbol{F}_1^{K'}(x'_R,y), \tag{45}$$

$$\boldsymbol{F}_2^{K'}(x_R,y) = -\omega^{-n_R} e^{i\chi''} \sigma_z \boldsymbol{F}_1^{K}(x'_R,y), \tag{46}$$

with $n_R = N_R - l_R - 1$ and $x'_R = x_R + l_R a$.

For states with k, the conditions are rewritten as

$$\boldsymbol{F}_{2k}^K(x_L) = -\omega^{+n_L} e^{i\chi'} \sigma_z U_L^{K'} \boldsymbol{F}_{1k}^{K'}(x_L), \tag{47}$$

$$\boldsymbol{F}_{2k}^{K'}(x_L) = -\omega^{-n_L} e^{i\chi''} \sigma_z U_L^{K} \boldsymbol{F}_{1k}^{K}(x_L), \tag{48}$$

$$\boldsymbol{F}_{2k}^K(x_R) = -\omega^{+n_R} e^{i\chi'} \sigma_z U_R^{K'} \boldsymbol{F}_{1k}^{K'}(x_R), \tag{49}$$

$$\boldsymbol{F}_{2k}^{K'}(x_R) = -\omega^{-n_R} e^{i\chi''} \sigma_z U_R^{K} \boldsymbol{F}_{1k}^{K}(x_R). \tag{50}$$

Then, eliminating the components of the top layers, we have a set of equations for $\boldsymbol{F}_{1k}^K(x_R)$, $\boldsymbol{F}_{1k}^{K'}(x_R)$, $\boldsymbol{F}_{1k}^K(x_L)$, and $\boldsymbol{F}_{1k}^{K'}(x_L)$. The condition for the presence of a nontrivial solution gives

$$\begin{vmatrix} U_L^K & 0 & 0 & \omega^{n_L-n_R} e^{-i\chi''}\sigma_z \\ 0 & \sigma_z & \omega^{n_L-n_R} e^{i\chi'} U_L^{K'} & 0 \\ U_R^K U_{11}^K & U_R^K U_{12}^K & e^{-i\chi''}\sigma_z U_{11}^{K'} & e^{-i\chi''}\sigma_z U_{12}^{K'} \\ \sigma_z U_{21}^K & \sigma_z U_{22}^K & e^{i\chi'} U_R^{K'} U_{21}^{K'} & e^{i\chi'} U_R^{K'} U_{22}^{K'} \end{vmatrix} = 0. \tag{51}$$

The band structure depends on $\omega^{n_L-n_R}$. We have

$$n_L - n_R = N - 3(N_R - N_L), \tag{52}$$

with $N = 2(N_R - N_L) + l_L + l_R$, showing that $\omega^{n_L-n_R} = \omega^\nu$, where integer ν is defined in Eq. (1). Therefore, the energy bands of the collapsed tube naturally depend on whether the tube is metallic or semiconducting before collapsing.

Equation (33) does not explicitly contain lattice constant a or ratio L/a and the same is true of Eq. (51) except for integer ν (=0, ±1) determining whether a nanotube is metallic or semiconducting before collapsing. This is, of course, the direct result of the use of the effective-mass scheme. Energy bands of collapsed nanotubes become a function of $2\pi\gamma/(\gamma_1 L)$, which is the ratio between $2\pi\gamma/L$ characterizing the energy scale in a cylindrical nanotube and γ_1 characterizing that in a bilayer graphene, and also a function of L_{F}/L.

IV. INTERLAYER POTENTIAL

As has been previously shown, the effective interlayer potential can be expressed as [54]

$$V_K(\boldsymbol{r}) = \begin{pmatrix} V_{AA}^K(\boldsymbol{r}) & V_{AB}^K(\boldsymbol{r}) \\ V_{BA}^K(\boldsymbol{r}) & V_{BB}^K(\boldsymbol{r}) \end{pmatrix} \tag{53}$$

for the K point, for example, with

$$V_{AA}^K = \frac{e^{-i\chi_{12}}}{N} \sum_{\boldsymbol{R}_{A1},\boldsymbol{R}_{A2}} \frac{1}{2}[g(\boldsymbol{r}-\boldsymbol{R}_{A1}) + g(\boldsymbol{r}-\boldsymbol{R}_{A2})] \times V(\boldsymbol{R}_{A1},\mathbf{R}_{A2}) e^{-i\boldsymbol{K}\cdot(\boldsymbol{R}_{A1}-\boldsymbol{R}_{A2})}, \tag{54}$$

$$V_{AB}^K = \frac{-e^{-i\chi_{12}}}{\omega^{-1}e^{-i\eta}N} \sum_{\boldsymbol{R}_{A1},\boldsymbol{R}_{B2}} \frac{1}{2}[g(\boldsymbol{r}-\boldsymbol{R}_{A1}) + g(\boldsymbol{r}-\boldsymbol{R}_{B2})] \times V(\boldsymbol{R}_{A1},\mathbf{R}_{B2}) e^{-i\boldsymbol{K}\cdot(\boldsymbol{R}_{A1}-\boldsymbol{R}_{B2})}, \tag{55}$$

$$V_{BA}^K = \frac{-e^{-i\chi_{12}}}{\omega e^{i\eta}N} \sum_{\boldsymbol{R}_{B1},\boldsymbol{R}_{A2}} \frac{1}{2}[g(\boldsymbol{r}-\boldsymbol{R}_{B1}) + g(\boldsymbol{r}-\boldsymbol{R}_{A2})] \times V(\boldsymbol{R}_{B1},\mathbf{R}_{A2}) e^{-i\boldsymbol{K}\cdot(\boldsymbol{R}_{B1}-\boldsymbol{R}_{A2})}, \tag{56}$$

$$V_{BB}^K = \frac{e^{-i\chi_{12}}}{N} \sum_{\boldsymbol{R}_{B1},\boldsymbol{R}_{B2}} \frac{1}{2}[g(\boldsymbol{r}-\boldsymbol{R}_{B1}) + g(\boldsymbol{r}-\boldsymbol{R}_{B2})] \times V(\boldsymbol{R}_{B1},\mathbf{R}_{B2}) e^{-i\boldsymbol{K}\cdot(\boldsymbol{R}_{B1}-\boldsymbol{R}_{B2})}, \tag{57}$$

where $2N$ is the number of carbon atoms contained in a unit cell of the nanotube and $g(\boldsymbol{r})$ is the smoothing function which varies smoothly in the range $|\boldsymbol{r}| \lesssim a$ and diminishes rapidly for $|\boldsymbol{r}| \gg a$. It should satisfy the condition

$$\sum_{\boldsymbol{R}_A} g(\boldsymbol{r}-\boldsymbol{R}_A) = \sum_{\boldsymbol{R}_B} g(\boldsymbol{r}-\boldsymbol{R}_B) = 1, \tag{58}$$

$$\int g(\boldsymbol{r}-\boldsymbol{R}_A)d\boldsymbol{r} = \int g(\boldsymbol{r}-\boldsymbol{R}_B)d\boldsymbol{r} = \Omega_0, \tag{59}$$

with $\Omega_0 = \sqrt{3}a^2/2$. We can use a Gaussian function $g(r) \propto \exp(-r^2/d^2)$ with range d, for example. Then, actual numerical calculations show that the effective potential becomes independent of $\boldsymbol{r}$ for $d \gtrsim a$. In the following, we can safely assume that $V^K(\boldsymbol{r})$ is independent of $\boldsymbol{r}$ and depends only on $\boldsymbol{\xi}$. The interlayer potential for the K' point can be obtained from V_K, using the time-reversal symmetry as shown in Appendix A.

In armchair tubes with $\eta = \pi/6$, we have

$$V_K(\xi) = e^{-i\chi}\begin{pmatrix} u(\xi) & +i\,v(\xi) \\ -i\,w(\xi) & u(\xi) \end{pmatrix}, \tag{60}$$

with real $u(\xi)$, $v(\xi)$, and $w(\xi)$, defined by

$$u(\xi) = \mathcal{U}(\xi), \tag{61}$$

$$v(\xi) = \mathcal{U}(\xi - 2a/\sqrt{3}), \tag{62}$$

$$w(\xi) = \mathcal{U}(\xi + 2a/\sqrt{3}), \tag{63}$$

where

$$\mathcal{U}(\xi)=\sum_{l_a,l_b} V(l_a\boldsymbol{a}+l_b\boldsymbol{b}-\boldsymbol{\xi})\exp\left[-\pi i l_a - \frac{2\pi i}{3}\left(l_b - \frac{l_a}{2}\right)\right], \tag{64}$$

with integers l_a and l_b. The time-reversal symmetry gives $V_{K'}(\xi) = V_K(\xi)$.

For actual numerical calculations, the interlayer hopping integral $V(\boldsymbol{R}_1,\boldsymbol{R}_2)$ is chosen as [78,79,88–93]

$$\begin{aligned} V(\boldsymbol{R}_1,\boldsymbol{R}_2) = {} & \frac{\alpha\gamma_1}{|\boldsymbol{t}|^2}\exp\left(-\frac{|\boldsymbol{t}|-c/2}{\delta}\right)(\boldsymbol{p}_1\cdot\boldsymbol{t})(\boldsymbol{p}_2\cdot\boldsymbol{t}) \\ & - \gamma_0\exp\left(-\frac{t-b}{\delta}\right)[(\boldsymbol{p}_1\cdot\boldsymbol{u})(\boldsymbol{p}_2\cdot\boldsymbol{u}) \\ & + (\boldsymbol{p}_1\cdot\boldsymbol{v})(\boldsymbol{p}_2\cdot\boldsymbol{v})], \end{aligned} \tag{65}$$

where b is the distance between neighboring carbons in graphene, given by $b = a/\sqrt{3}$, c is the lattice constant along the c axis in graphite given by $c/a = 2.72$, and δ the decay rate of the π orbital. Further, γ_1 is the hopping integral between nearest-neighbor sites of neighboring layers in graphite ($\gamma_1 \sim 0.4$ eV). Vectors $\boldsymbol{p}_1$ and $\boldsymbol{p}_2$ are unit vectors directed along π orbitals at $\boldsymbol{R}_1$ and at $\boldsymbol{R}_2$, respectively, $\boldsymbol{t}$ is a vector connecting the two sites, and $\boldsymbol{u}$ and $\boldsymbol{v}$ unit vectors perpendicular to $\boldsymbol{t}$ and to each other. In the following numerical calculations, we use parameters $\gamma_1/\gamma_0 = 0.119$, $\delta/a = 0.185$, and $\alpha = 1.4$. Figure 5 shows the effective potentials $u(\xi)$, $v(\xi)$, and $w(\xi)$ for $d/a = 1$.

In this geometry, it is convenient to choose $\chi(\xi) = 0$ because both Hamiltonian and boundary conditions contain phase χ only, where χ is defined in Eqs. (20) and (15). The Hamiltonian is written as

$$\mathcal{H}_K = \begin{pmatrix} \gamma(\boldsymbol{\sigma}\cdot\hat{\boldsymbol{k}}) & u\sigma_0 + \frac{i}{2}(v-w)\sigma_x - \frac{1}{2}(v+w)\sigma_y \\ u\sigma_0 - \frac{i}{2}(v-w)\sigma_x - \frac{1}{2}(v+w)\sigma_y & \gamma(\boldsymbol{\sigma}\cdot\hat{\boldsymbol{k}}) \end{pmatrix}, \tag{66}$$

with (2,2) unit matrix σ_0. Using unitary matrix

$$U = \frac{1}{\sqrt{2}}\begin{pmatrix} \sigma_0 & \sigma_0 \\ \sigma_0 & -\sigma_0 \end{pmatrix}, \tag{67}$$

the Hamiltonian is transformed into

$$U\mathcal{H}^K U^\dagger = \begin{pmatrix} \gamma(\boldsymbol{\sigma}\cdot\hat{\boldsymbol{k}}) + u\sigma_0 - \frac{1}{2}(v+w)\sigma_y & -\frac{i}{2}(v-w)\sigma_x \\ \frac{i}{2}(v-w)\sigma_x & \gamma(\boldsymbol{\sigma}\cdot\hat{\boldsymbol{k}}) - u\sigma_0 + \frac{1}{2}(v+w)\sigma_y \end{pmatrix}. \tag{68}$$

As shown in Fig. 5, we have $u = \gamma_1$, $v = 0$, and $w = 0$ for $\xi = 0$. The effective Hamiltonian (66) becomes that of an AA-stacked bilayer graphene with interlayer interaction γ_1. Equation (68) shows that the energy bands consist of two copies of the band in monolayer graphene, one shifted in energy by $+\gamma_1$ and the other by $-\gamma_1$.

When $\xi/(\sqrt{3}a) = \frac{1}{3}$, Fig. 5 shows that $u = v = 0$, $w/\gamma_1 = 1$. The effective Hamiltonian (66) becomes that of an AB-stacked bilayer graphene with interlayer interaction γ_1 multiplied by extra phases $+i$ or $-i$,

$$\mathcal{H}_K = \begin{pmatrix} \gamma(\boldsymbol{\sigma}\cdot\hat{\boldsymbol{k}}) & -\frac{i}{2}\gamma_1\sigma_- \\ \frac{i}{2}\gamma_1\sigma_+ & \gamma(\boldsymbol{\sigma}\cdot\hat{\boldsymbol{k}}) \end{pmatrix}, \tag{69}$$

with $\sigma_\pm = \sigma_x \pm i\sigma_y$. This occurs also for $\xi/(\sqrt{3}a) = \frac{2}{3}$, although the interlayer interaction is present between a

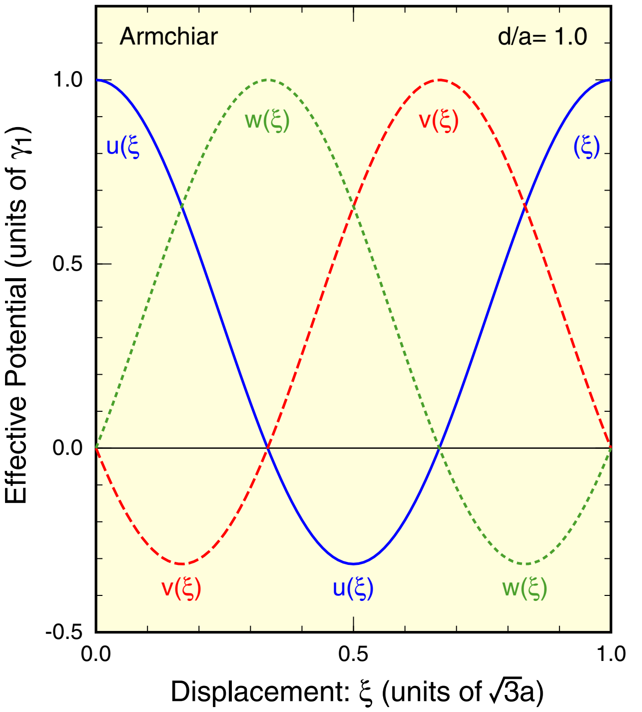

FIG. 5. An example of interlayer potentials $u(\xi)$, $v(\xi)$, and $w(\xi)$ calculated numerically for the displacement in the armchair direction.

different pair because $u = w = 0$ and $v = \gamma_1$ and therefore the off-diagonal elements in the above Hamiltonian should be exchanged with each other.

At the mid point $\xi/(\sqrt{3}a) = \frac{1}{2}$ (mid-period), we have $w = v > 0$ and $u < 0$. The numerical calculation gives $u/\gamma_1 = -0.314\ldots$ and $v/\gamma_1 = w/\gamma_1 = 0.655\ldots$. Thus, the energy bands for this mid-period structure consist of two independent Weyl cones, as shown in Eq. (68). The cone at $(k_y,\varepsilon) = (0,+\gamma_1)$ in the AA stacking structure moves to $(k_y,\varepsilon) = (+v/\gamma, -|u|)$, i.e., to the right-hand side in the k_y direction and to the negative energy region. The cone at $(0,-\gamma_1)$ in the AA stacking structure moves to $(-v/\gamma, +|u|)$, i.e., to the left-hand side in the k_y direction and to the positive energy region. This is illustrated in Fig. 6.

In the regions $0 < \xi/(\sqrt{3}a) < \frac{1}{3}$ and $\frac{2}{3} < \xi/(\sqrt{3}a) < 1$, condition $u(\xi)^2 - v(\xi)w(\xi) > 0$ is satisfied because $v(\xi)w(\xi) < 0$ as shown in Fig. 5. There are two conelike bands in the vicinity of zero energy at $\boldsymbol{k} = (\pm k_0,0)$, with

$$k_0 = \frac{\sqrt{u^2 - vw}}{\gamma} \leqslant \frac{\gamma_1}{\gamma}. \tag{70}$$

In the following, we shall confine ourselves to the case $0 < \xi/(\sqrt{3}a) < \frac{1}{3}$ for which $v(\xi) < 0$ and $w(\xi) > 0$. Extension to the case $\frac{2}{3} < \xi/(\sqrt{3}a) < 1$ is straightforward.

Let us define

$$\tan\psi_1 = \frac{w}{\gamma k_0 + u}, \quad \tan\psi_2 = \frac{-v}{\gamma k_0 + u}, \tag{71}$$

giving $\psi_1 > \psi_2$, because $w > -v$ as shown in Fig. 5. Then, wave functions corresponding to eigenstates of the velocity in the x direction are given as follows:

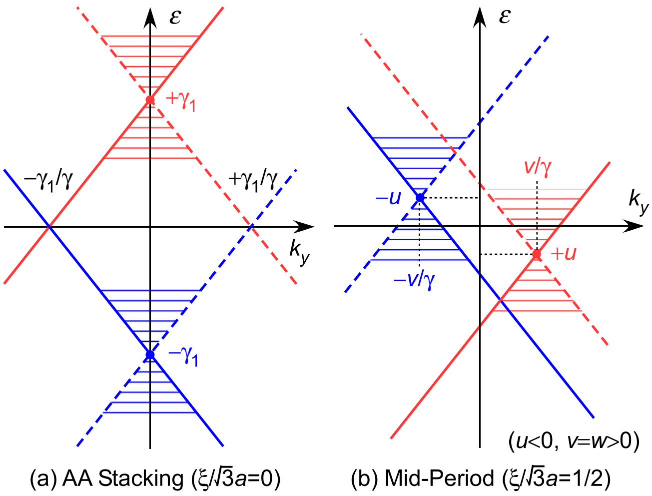

(a) AA Stacking (ξ/√3a=0) (b) Mid-Period (ξ/√3a=1/2)

FIG. 6. The correspondence between the band structure of a bilayer graphene with AA stacking and the mid-period displacement in the armchair direction. Two linear bands given by the (red and blue) solid lines survive in collapsed nanotubes.

$$\boldsymbol{F}^{(+)}_{+k_0}(\boldsymbol{r}) = \frac{1}{2}\begin{pmatrix} +\sin\psi_1 + i\cos\psi_2 \\ +i\cos\psi_1 + \sin\psi_2 \\ -i\cos\psi_1 + \sin\psi_2 \\ +\sin\psi_1 - i\cos\psi_2 \end{pmatrix} e^{+i\,k_0 x}, \tag{72}$$

$$\boldsymbol{F}^{(-)}_{+k_0}(\boldsymbol{r}) = \frac{1}{2}\begin{pmatrix} +\sin\psi_1 - i\cos\psi_2 \\ +i\cos\psi_1 - \sin\psi_2 \\ -i\cos\psi_1 - \sin\psi_2 \\ +\sin\psi_1 + i\cos\psi_2 \end{pmatrix} e^{+i\,k_0 x}, \tag{73}$$

$$\boldsymbol{F}^{(+)}_{-k_0}(\boldsymbol{r}) = \frac{1}{2}\begin{pmatrix} -\sin\psi_1 - i\cos\psi_2 \\ -i\cos\psi_1 - \sin\psi_2 \\ -i\cos\psi_1 + \sin\psi_2 \\ +\sin\psi_1 - i\cos\psi_2 \end{pmatrix} e^{-i\,k_0 x}, \tag{74}$$

$$\boldsymbol{F}^{(-)}_{-k_0}(\boldsymbol{r}) = \frac{1}{2}\begin{pmatrix} -\sin\psi_1 + i\cos\psi_2 \\ -i\cos\psi_1 + \sin\psi_2 \\ -i\cos\psi_1 - \sin\psi_2 \\ +\sin\psi_1 + i\cos\psi_2 \end{pmatrix} e^{-i\,k_0 x}, \tag{75}$$

where (+) and (−) denote those with positive and negative velocities, respectively. Then, the effective Hamiltonian in the vicinity of $\boldsymbol{k} = (\pm k_0,0)$ becomes

$$\mathcal{H}_{\text{eff}} = \begin{pmatrix} +\alpha_x\hat{k}_x & \alpha_y\hat{k}_y \\ \alpha_y\hat{k}_y & -\alpha_x\hat{k}_x \end{pmatrix} + \beta\hat{k}_y, \tag{76}$$

with

$$\alpha_x = \gamma\cos(\psi_1 - \psi_2), \tag{77}$$

$$\alpha_y = \tfrac{1}{2}\gamma\,(\sin 2\psi_1 + \sin 2\psi_2), \tag{78}$$

$$\beta = \tfrac{1}{2}\gamma\,(\sin 2\psi_1 - \sin 2\psi_2), \tag{79}$$

where $\hat{k}_x$ is measured from $\pm k_0$.

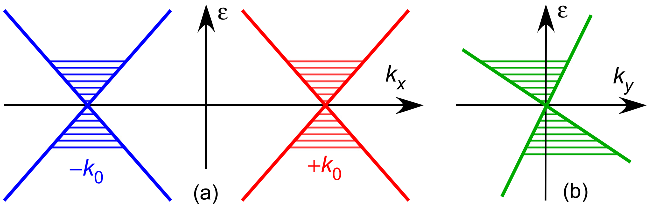

FIG. 7. A schematic illustration of tilted Weyl cones at zero energy in bilayer graphene displaced in the armchair direction. $0 < \xi/(\sqrt{3}a) < \frac{1}{3}$.

This Hamiltonian corresponds to a Weyl cone, tilted in the negative k_y direction and anisotropic. In fact, the energy bands become

$$\varepsilon(k_x,k_y) = \pm\sqrt{\alpha_x^2 k_x^2 + \alpha_y^2 k_y^2} + \beta k_y. \tag{80}$$

This is illustrated in Fig. 7. For the K' point, we should replace β with $-\beta$, and the tilt direction becomes opposite.

The parameters characterizing the tilted Weyl cones are shown in Fig. 8. With the increase of ξ, the position k_0 of the cone gradually decreases from γ_1/γ and rapidly vanishes at $\xi/(\sqrt{3}a) = \frac{1}{3}$. Furthermore, α_x stays almost the same as γ, and α_y increases almost linearly with ξ for small ξ, showing significant anisotropy between the x and y directions. The tilt parameter β increases slowly and remains smaller than α_y. Near $\xi/(\sqrt{3}a) = \frac{1}{3}$, the Weyl cone becomes almost symmetric because $\alpha_x \approx \alpha_y \gg \beta$, but it disappears at $\xi/(\sqrt{3}a) = \frac{1}{3}$ because all the parameters vanish there.

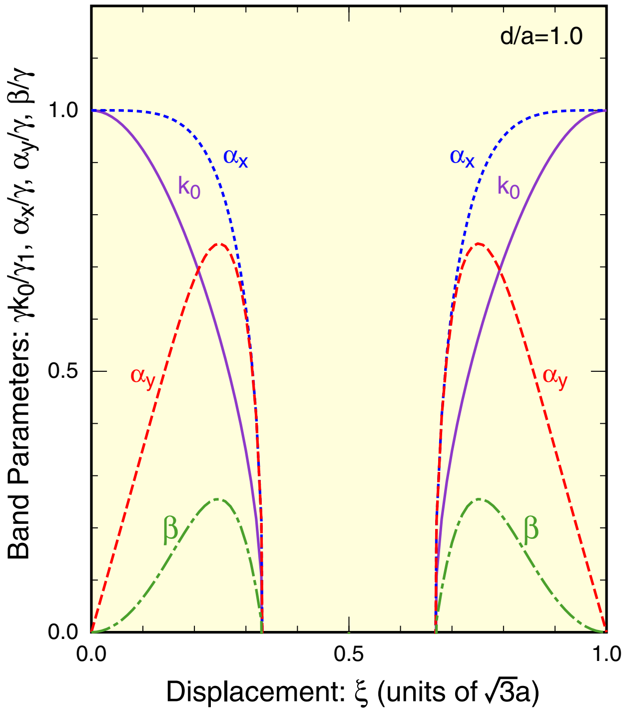

FIG. 8. The band parameters characterizing tilted Weyl cones at zero energy in bilayer graphene displaced in the armchair direction.

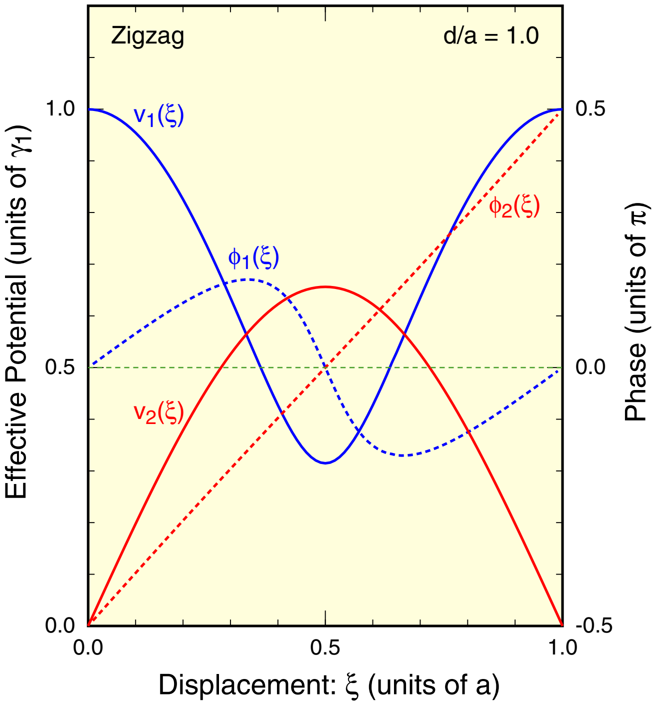

FIG. 9. Effective interlayer potentials $v_1(\xi)$ and $v_2(\xi)$ and their phases $\phi_1(\xi)$ and $\phi_2(\xi)$ calculated numerically for zigzag displacement.

In zigzag tubes with $\eta = 0$, we have

$$V_K = e^{-i\chi_{12}}\begin{pmatrix} v_1(\xi)e^{+i\phi_1(\xi)} & v_2(\xi)e^{+i\phi_2(\xi)} \\ v_2(\xi)e^{+i\phi_2(\xi)} & v_1(\xi)e^{+i\phi_1(\xi)} \end{pmatrix}, \tag{81}$$

with real $v_1(\xi)$, $v_2(\xi)$, $\phi_1(\xi)$, and $\phi_2(\xi)$ for the K point. The time-reversal symmetry gives

$$V_{K'} = e^{-i\chi_{12}}e^{2\pi i(\xi/a)}\begin{pmatrix} v_1(\xi)e^{-i\phi_1(\xi)} & -v_2(\xi)e^{-i\phi_2(\xi)} \\ -v_2(\xi)e^{-i\phi_2(\xi)} & v_1(\xi)e^{-i\phi_1(\xi)} \end{pmatrix} \tag{82}$$

for the K' point. In the above we have set $\boldsymbol{\xi} = \xi\boldsymbol{a}/a$.

Figure 9 shows $v_1(\xi)$, $v_2(\xi)$, $\phi_1(\xi)$, and $\phi_2(\xi)$ numerically calculated. For $\xi = 0$, we have $v_1 = \gamma_1$ and $v_2 = 0$, corresponding to an AA-stacked bilayer with interlayer interaction γ_1. For $\xi/a = \frac{1}{2}$ (mid-period), all the components become real except a common phase factor and are numerically given by $v_1/\gamma_1 = 0.314\ldots$ and $v_2/\gamma_1 = 0.655\ldots$. In this case, the Hamiltonian is block diagonalized into a pair of (2,2) matrices and becomes

$$\mathcal{H}^K = \begin{pmatrix} \mathcal{H}_+^K & 0 \\ 0 & \mathcal{H}_-^K \end{pmatrix}, \quad \mathcal{H}^{K'} = \begin{pmatrix} \mathcal{H}_+^{K'} & 0 \\ 0 & \mathcal{H}_-^{K'} \end{pmatrix}, \tag{83}$$

with

$$\mathcal{H}_\pm^K = \mathcal{H}_0^K \pm v_1\sigma_0 \pm v_2\sigma_x, \tag{84}$$

$$\mathcal{H}_\pm^{K'} = \mathcal{H}_0^{K'} \mp v_1\sigma_0 \pm v_2\sigma_x, \tag{85}$$

where the common phase factor $\chi_{12} = 0$ is chosen. Thus, the energy bands for the mid-period structure consist of two independent cones, shifted in both energy and k_x directions, exactly the same as those for $\xi/(\sqrt{3}a)=\frac{1}{2}$ in the armchair case, although the k_x and k_y directions are exchanged.

V. BAND STRUCTURE

A. Armchair nanotube

Figure 10 shows some examples of the band structure of the bilayer graphene displaced in the armchair direction. As the top layer is gradually displaced from $\xi=0$ shown in Fig. 10(a), the electronic states in the lower cone hybridize with upper cone. As a result, an eye-shaped stateless region along the k_x direction is created near zero energy, and two tilted Weyl cones are formed at zero energy, as mentioned above. These cones shift toward $k_x=0$ with the increase in ξ as shown in Figs. 10(b) for $\xi/(\sqrt{3}a)=\frac{1}{12}$ and 10(c) for $\frac{1}{4}$.

When $\xi/(\sqrt{3}a)=\frac{1}{3}$ corresponding to an AB-stacked bilayer graphene, these two Weyl cones merge at $k_x=0$ and two parabolic bands consisting of bonding and antibonding states touch at zero energy, as shown in Fig. 10(d). With the further increase in the displacement, two crossing points reappear on the plane $k_x=0$, as in Fig. 10(e) for $\xi/(\sqrt{3}a)=\frac{5}{12}$. The crossing point with $k_y<0$ is shifted upward in energy and that with $k_y>0$ is shifted downward. When $\xi/(\sqrt{3}a)=\frac{1}{2}$ (mid period) shown in Fig. 10(f), two conelike bands shifted in both energy and k_y directions become independent of each other. When we increase ξ from $\xi/(\sqrt{3}a)=\frac{1}{2}$ to 1, the band structure changes from Fig. 10(f) back to Fig. 10(a), as shown in the insets.

This change in the band structure as a function of ξ manifests itself in that of corresponding collapsed nanotubes. By Eq. (33), we can determine k_x in the bilayer region for given k along the axis direction and energy. In fact, in the vicinity of zero energy, electron wave with k_x is reflected into $-k_x$ at the right edge and that with $-k_x$ into k_x at the left edge. Roughly speaking, the energy bands $\varepsilon(k)$ in collapsed nanotubes with a wide flattened region are understood in terms of $\varepsilon(k_x,k)$ of the corresponding bilayer with appropriately discretized k_x, unless k_x strongly depends on k.

For $\xi=0$ with AA stacking [shown in Fig. 10(a)], at $k_x=0$ and $k_y\approx\pm\gamma_1/\gamma$, there are two sets of states crossing at zero energy with linear dependence on k_y, i.e.,

$$\varepsilon_{st}(k_y)=s\,\gamma|k_y|+t\,\gamma_1, \tag{86}$$

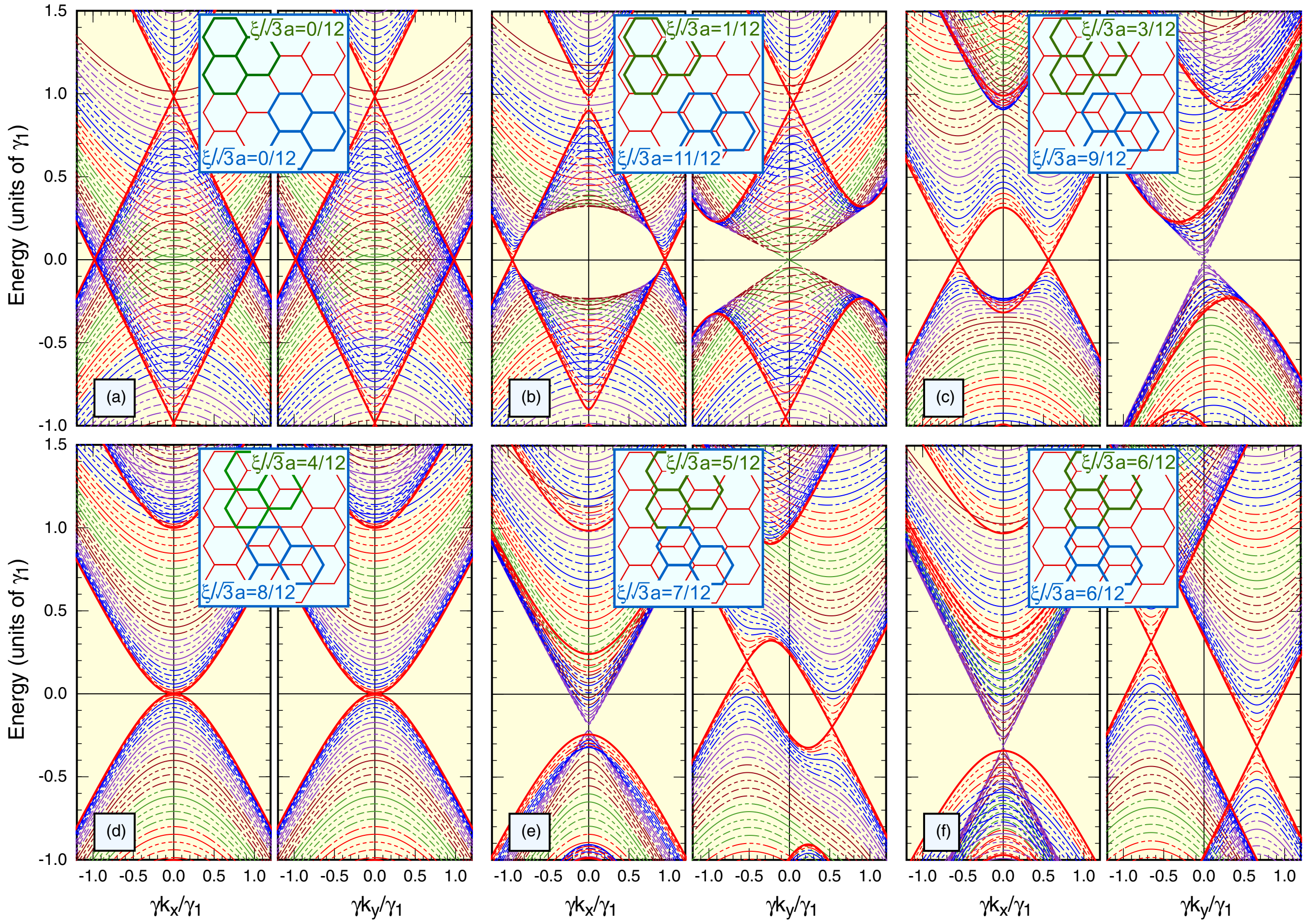

FIG. 10. Some examples of the band structure of a bilayer graphene displaced in the armchair direction. In each of the left figures, the energy $\varepsilon(\boldsymbol{k})$ is plotted against k_x for positive k_y with interval $\Delta k_y=0.05\times(\gamma_1/\gamma)$, and in right figures against k_y for positive k_x with interval $\Delta k_x=0.05\times(\gamma_1/\gamma)$. The lattice structure is illustrated in the insets. (a) $\xi/(\sqrt{3}a)=0$ or 1. (b) $\frac{1}{12}$ or $\frac{11}{12}$. (c) $\frac{3}{12}$ or $\frac{9}{12}$. (d) $\frac{4}{12}$ or $\frac{8}{12}$. (e) $\frac{5}{12}$ or $\frac{7}{12}$. (f) $\frac{6}{12}$.

with $s = \pm 1$ and $t = \pm 1$. As discussed in Appendix B 2, only two states corresponding to $+\gamma k_y + \gamma_1$ and $-\gamma k_y - \gamma_1$ satisfy the boundary conditions at the left and right edges in the limit of narrow curved region $L_C/L \ll 1$. The allowed linear bands are denoted by solid lines in Fig. 6. With the increase of L_C, these bands are shifted to the right-hand side by $(\gamma_1/\gamma)(L_C/L_F) \approx (\gamma_1/\gamma)(L_C/L)$. A corresponding result in the opposite limit of small L_F/L has been obtained by perturbational treatment of interlayer interaction in Ref. [54].

For $\xi/(\sqrt{3}a) = \frac{1}{2}$ (mid-period) shown in Fig. 10(f), there are two crossing bands having a linear dispersion for $k_x = 0$, shifted in both energy and wave vector k_y. The correspondence to the bands in the AA stacking is shown in Fig. 6. Among these bands, two bands denoted by solid lines in Fig. 6(b) satisfy the boundary conditions at both edges and survive in the corresponding collapsed nanotube, although being shifted toward $k = 0$ for nonzero L_C.

For $\xi/(\sqrt{3}a) = \frac{1}{3}$ with AB stacking structure shown in Fig. 10(d), there are two parabolic bands $\varepsilon_\pm(k_y) = \pm\gamma^2 k_y^2/\gamma_1$, touching together at zero energy for $k_x = 0$. As shown in Appendix B 3, only the conduction band $\varepsilon_+(k_y)$ satisfies the boundary conditions at the right and left edges, and the valence band $\varepsilon_-(k_y)$ does not. As a result, the conduction band bottom remains at zero energy, while the valence band is shifted downward, opening up a gap. The reason lies in the fact that the wave functions of the bottom and top layers have opposite signs for the conduction band, while they have the same sign for the valence band. As already mentioned, the wave functions of the π orbital changes its sign, when they are connected through the circular monolayer region. This result has also been obtained for small L_F by a perturbational treatment of interlayer interaction in Ref. [54].

In the region $0 < \xi/(\sqrt{3}a) < \frac{1}{3}$, shown in Figs. 10(b) and 10(c), in general, band gaps are opened between conduction and valence bands due to interlayer interactions. However, this general feature can be strongly modified in narrow regions of ξ for tubes with sufficiently large L_F. This occurs due to interferences between two tilted Weyl cones at $(\pm k_0, 0)$, where k_0 is given in Eq. (70). As discussed in Appendix B 4, the state with k_0 is reflected into that with $-k_0$ at the right edge and that with $-k_0$ into that with $+k_0$ at the left edge. There is no reflection within each of the $+k_0$ and $-k_0$ bands. When

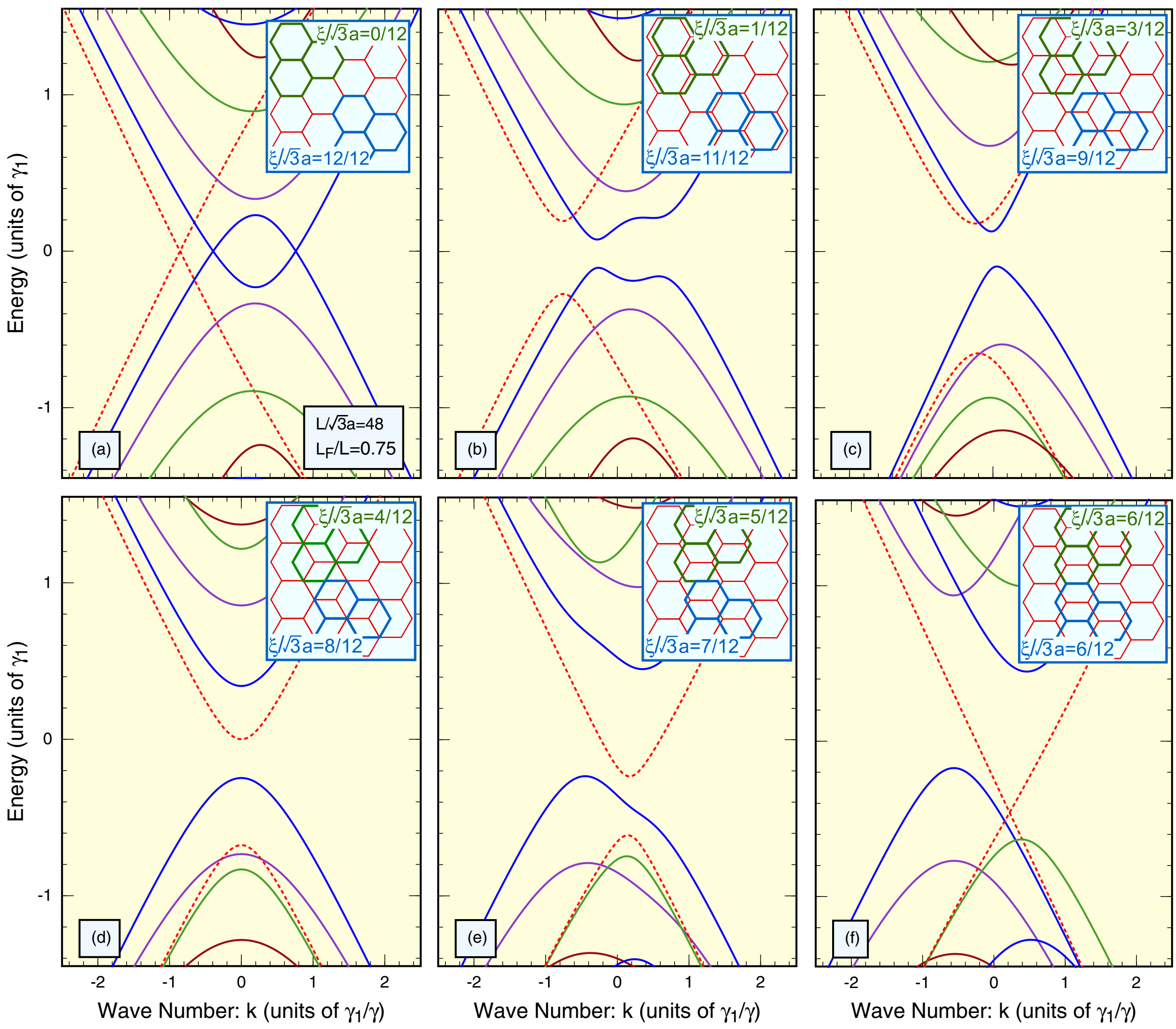

FIG. 11. Calculated band structure of collapsed nanotubes with $L/(\sqrt{3}a) = 48$ and $L_F/L = 0.75$ with displacement ξ in armchair direction. Red dotted lines show linear dispersions at AA stacking and the change with the displacement.

resonance condition $k_0 L_F = 2\pi j$ with integer j is satisfied, a set of linear bands crossing at zero energy appears, i.e.,

$$\varepsilon_\pm(k) = \pm\alpha_y|k| + \beta k, \tag{87}$$

where α_y and β are shown in Fig. 8. These linearly crossing bands can appear when $L_F > L_F^{\rm min}$, with $L_F^{\rm min} = 2\pi\gamma/\gamma_1$, because $k_0 \leqslant \gamma_1/\gamma$ as in Eq. (70). In the present case, we have $L_F^{\rm min}/(\sqrt{3}a) \approx 26.4$.

In the region $\frac{1}{3} < \xi/(\sqrt{3}a) < \frac{1}{2}$, shown in Fig. 10(e), band gaps are opened between conduction and valence bands due to interlayer interactions. However, because of the strong asymmetry between positive and negative k_y, some conduction and valence bands may overlap in energy, making the collapsed nanotube semimetallic.

Figure 11 shows some examples of calculated energy bands of a collapsed nanotube with $L/(\sqrt{3}a) = 48$ and $L_F/L = 0.75$ or $L_F/(\sqrt{3}a) = 36$. Only the band structure near the K point is shown, while that near the K' point is given by inversion in the k direction. For $\xi = 0$ with AA stacking, shown in Fig. 11(a), only a pair of a linearly crossing bands denoted by the dotted lines survives while the other pair is destroyed. These crossing bands are shifted by $\sim(\gamma_1/\gamma)(L_C/L_F)$ to the positive k direction as has been discussed above. When $\xi/(\sqrt{3}a)$ is varied from zero to $\frac{1}{2}$, these bands continuously change as shown by the dotted lines in Figs. 11(a)–11(f). Other bands are understood roughly by appropriately discretized k_x in the band structure of the AA stacked bilayer.

With the increase of ξ, as shown in Fig. 11(b) corresponding to $\xi/(\sqrt{3}a) = \frac{1}{12}$, for example, the crossing bands denoted by the dotted lines split into conduction and valence bands by a gap, and the collapsed tube becomes semiconducting. For $\xi/(\sqrt{3}a) = \frac{1}{4}$ shown in Fig. 11(c), the bands given by the dotted lines overlap with other bands. In Figs. 11(b) and 11(c), the gap separating conduction and valence bands is no longer determined by those denoted by the dotted lines.

For $\xi/(\sqrt{3}a) = \frac{1}{3}$ with AB stacking in the bilayer region, shown in Fig. 11(d), the conduction-band minimum is at zero energy, while the valence bands are lowered, thus forming a band gap, as has been discussed above. For $\xi/(\sqrt{3}a) = \frac{5}{12}$ shown in Fig. 11(e), nonzero band gap is formed for each k value, but some of conduction and valence bands overlap in energy, and therefore the tube becomes semimetallic. For $\xi/(\sqrt{3}a) = \frac{1}{2}$ (mid-period) shown in Fig. 11(f), a set of crossing bands with near-linear dispersion is formed, although the crossing point is shifted toward the negative-energy side and toward the positive k direction. These correspond to two linear bands shown in Fig. 11(a) for $\xi = 0$, as has been discussed above (see also Fig. 6).

Figure 12 shows the band structures for (a) $\xi/(\sqrt{3}a) = 0.17$, (b) 0.19, and (c) 0.23, i.e., when ξ is in the range between (b) and (c) of Fig. 11. The band gap disappears and a set of linearly crossing bands is formed in the vicinity of zero energy in Fig. 12(b). This is the result of interference between two tilted Weyl cones at $\pm k_0$ discussed above. In fact, for $\xi/(\sqrt{3}a) = 0.19$ in Fig. 12(b), we have $\gamma k_0/\gamma_1 \approx 0.73$, $\alpha_x \approx 0.96$, $\alpha_y \approx 0.66$, and $\beta \approx 0.21$, according to Fig. 8. For these values of the parameters, the condition $k_0 L_F = 2\pi$ is satisfied and the linear-crossing bands in the vicinity of zero energy shown in Fig. 12(b) are well reproduced by Eq. (87).

B. Zigzag nanotube

Some examples of the band structure of bilayer graphenes displaced in the zigzag direction are shown in Fig. 13. For $\xi = 0$ corresponding to AA stacking shown in Figs. 13(a) and 13(d), two conelike bands same as in monolayer graphene are shifted in energy by $\pm\gamma_1$ and independent of each other. As the top layer is displaced from $\xi = 0$ as in Figs. 13(b) and 13(e) corresponding to $\xi/a = \frac{1}{4}$, two conelike crossing bands interacting with each other are formed for $k_y = 0$, but the crossing energy is shifted in the direction opposite

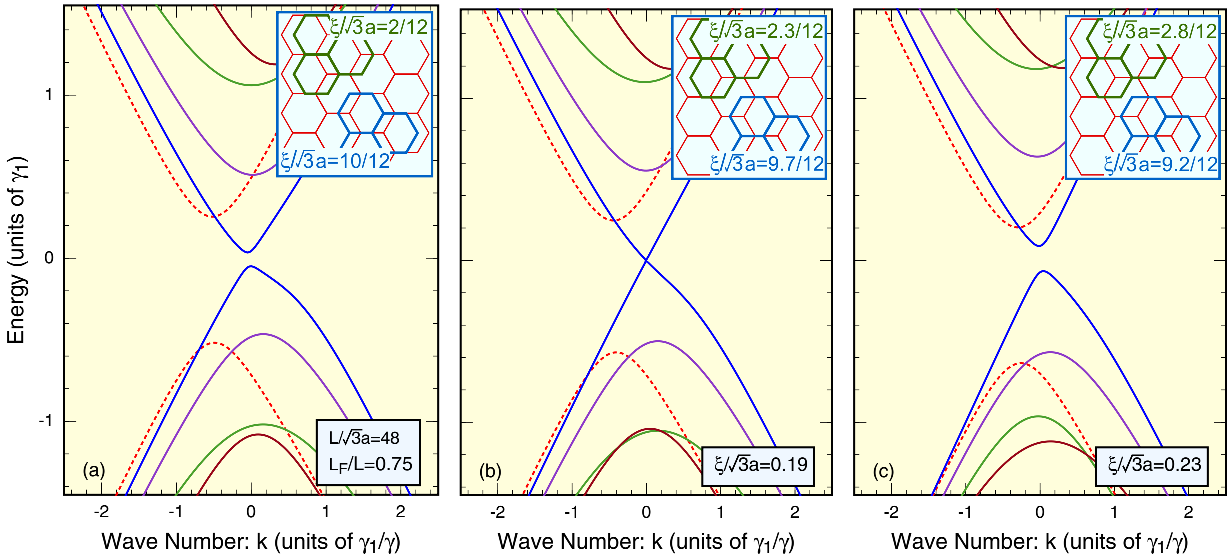

FIG. 12. Calculated band structure of collapsed nanotubes with $L/(\sqrt{3}a) = 48$, $L_F/L = 0.75$ having armchair structures. The band gap disappears and a set of linear-crossing bands emerges at zero energy for the displacement (b) $\xi/(\sqrt{3}a) = 0.19$.

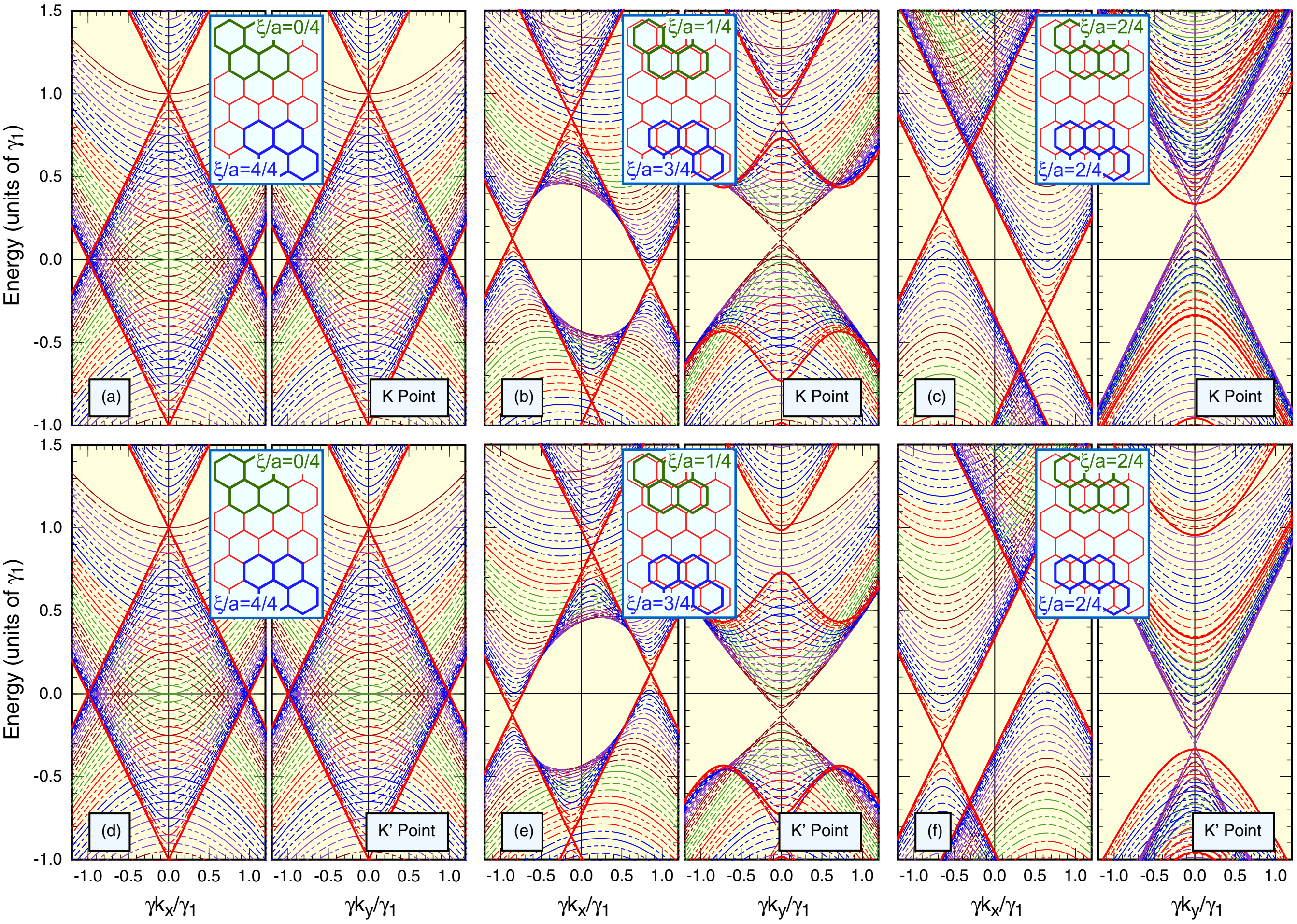

FIG. 13. Some examples of the band structure of a bilayer graphene displaced in the zigzag direction. In each of the left figures the energy $\varepsilon(\boldsymbol{k})$ is plotted against k_x for positive k_y with interval $\Delta k_y(\gamma_1/\gamma)^{-1} = 0.05$, and in right figures against k_y for positive k_x with interval $\Delta k_x(\gamma_1/\gamma)^{-1} = 0.05$. The lattice structure is illustrated in the insets. (a) K and (d) K' point [$\xi/a = 0/4$ or $4/4$]. (b) K and (e) K' point [$\xi/a = 1/4$ or $3/4$]. (c) K and (f) K' point [$\xi/a = 2/4$].

between positive and negative k_x and between the K and K' points. For $\xi/a = \frac{1}{2}$ (mid-period) shown in Figs. 13(c) and 13(f), these cones again become independent. In general, we have $\varepsilon_K(-k_x,k_y) = \varepsilon_{K'}(+k_x,k_y)$, $\varepsilon_K(k_x,-k_y) = \varepsilon_K(k_x,+k_y)$, and $\varepsilon_{K'}(k_x,-k_y) = \varepsilon_{K'}(k_x,+k_y)$.

This change in the band structure as a function of ξ again manifests itself in that of corresponding collapsed nanotubes. In a collapsed zigzag nanotube, an electron wave with $\pm k_x$ at the K point is dominantly reflected into that with $\mp k_x$ at the K' point having the same energy at the edges. The matching conditions for the phase of the wave function given by Eq. (51) determine k_x and the corresponding energy as a function of k. The dependence on k is not so strong in semiconducting nanotubes and metallic nanotubes other than those with AA stacked collapsed region. As a result, a very rough feature of the energy bands is again understood in terms of $\varepsilon_K(k_x,k)$ and $\varepsilon_{K'}(k_x,k)$ for discretized k_x. The only exception occurs in metallic nanotubes with AA stacking shown in Figs. 13(a) and 13(d). In fact, as discussed in Appendix B 5, there appears a pair of bands linear and crossing each other at $k = 0$ near $\varepsilon = \pm\gamma_1$, for which k_x satisfying Eq. (51) varies in proportion to k with coefficient of the order of ± 1.

Figure 14 shows some examples of calculated band structure for collapsed zigzag tubes with $L/a = 72$ and $L_F/L = 0.75$. In collapsed metallic tubes with AA stacking structure, given in Fig. 14(a), two pairs of linear-crossing bands are present around $\varepsilon \approx \pm\gamma_1$, and other bands are nearly parabolic but shifted in the positive and negative k directions, thus crossing each other at $k = 0$.

In collapsed semiconducting tubes with AA stacking, given in Fig. 14(d), each band is symmetric with respect to $k = 0$ and linear bands are completely absent near $k = 0$. For $0 < \xi/a < \frac{1}{2}$, as shown in Figs. 14(b) and 14(e) for $\xi/a = \frac{1}{4}$, for example, band gaps are opened near zero energy and collapsed nanotubes become semiconducting irrespective of the value of ν before being collapsed. For $\xi/a = \frac{1}{2}$ (mid-period) shown in Figs. 14(c) and 14(f), collapsed nanotubes become metallic independent of ν in the case of $L_F/L = 0.75$.

Some examples showing the dependence on L_F/L are presented in Fig. 15 for $\xi/a = \frac{1}{2}$ (mid-period). In metallic tubes with $\nu = 0$ shown for $L_F/L = 0.1$, 0.4, and 0.75 in Figs. 15(a), 15(d), and 14(c), respectively, a gap first opens up with the increase in L_F/L, takes a maximum, and then becomes smaller and vanishes. Only in the limit of small

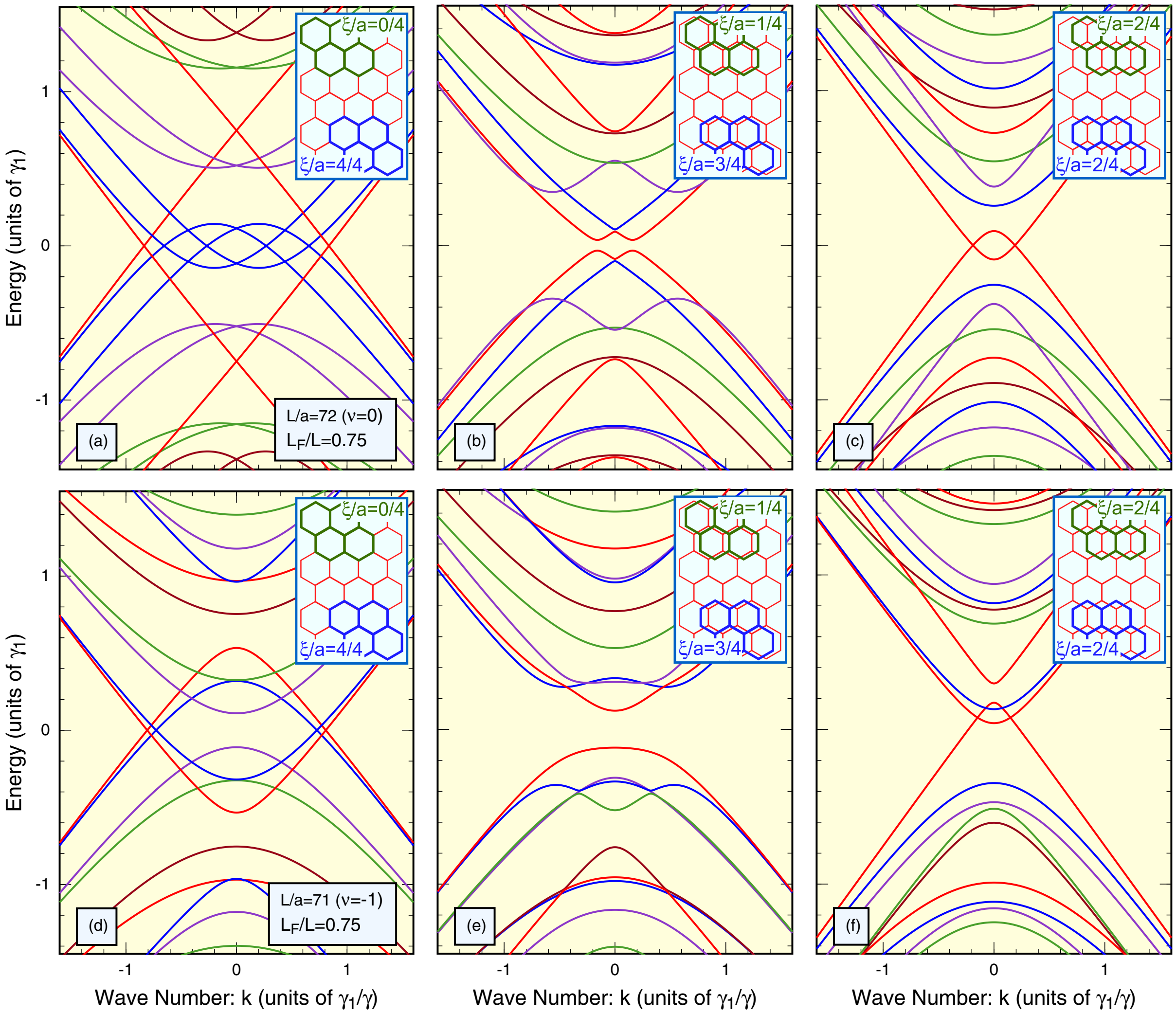

FIG. 14. Calculated band structure of collapsed nanotubes with $L_F/L = 0.75$ having zigzag structures. (a)–(c) $L/a = 72$ ($\nu = 0$). (d)–(f) $L/a = 71$ ($\nu = -1$).

L_F/L, the band structure is close to that of a cylindrical tube with a tiny gap at $\varepsilon = 0$.

For semiconducting tubes with $\nu = +1$ shown in Figs. 15(b) and 15(e) and with $\nu = -1$ shown in Figs. 15(c) and 15(f), the band overlapping present for $L_F/L = 0.75$ persists even for smaller $L_F/L = 0.4$, but eventually a band gap opens for $L_F/L = 0.1$, roughly corresponding to the semiconducting zigzag tube. For sufficiently wide zigzag tubes, the energy bands of collapsed case for $\nu = -1$ are obtained by inverting the energy axis for those with $\nu = +1$, although this correspondence is still not complete for $L/a = 71$ ($\nu = -1$) and for $L/a = 70$ ($\nu = +1$).

VI. DISCUSSION AND CONCLUSION

So far, we have completely neglected the presence of curvature in the monolayer region corresponding to the closed edge. A typical diameter of the curved region is estimated (sometimes assumed) to be of the order of that in narrow single-wall nanotubes according to various theoretical investigations [25,33–52]. Recent density-functional calculations give diameter of about 0.854 nm [53], slightly larger than that of a (6,6) single-wall nanotube. Effects of such curvature can be described by a local shift in the wave vector or an effective vector potential in the curved region in the effective-mass scheme [17,94].

In a cylindrical nanotube, the curvature is represented by an effective magnetic flux passing through the cross section, which has opposite signs between the K and K' points, resulting in a shift in the energy bands. The presence of small shifts has long been known to be present in various first-principles calculations in narrow single-wall nanotubes [5,6]. Combined with the presence of a trigonal warping of the band in graphene [95], the curvature constitutes one important origin leading to the so-called family behavior of optical spectra [96–98]. In principle, effects of the curvature can be included in our calculations once the actual form of the cross section is established. This problem is left for a future study.

We have assumed that the relative displacement or sliding of two layers can take any value in the bilayer region in a collapsed nanotube. This is valid because first-principles calculations in bilayer graphenes show that the energy difference by sliding is much smaller than the average thermal energy at room temperature [99,100]. Actually, AB, AA, displaced, and

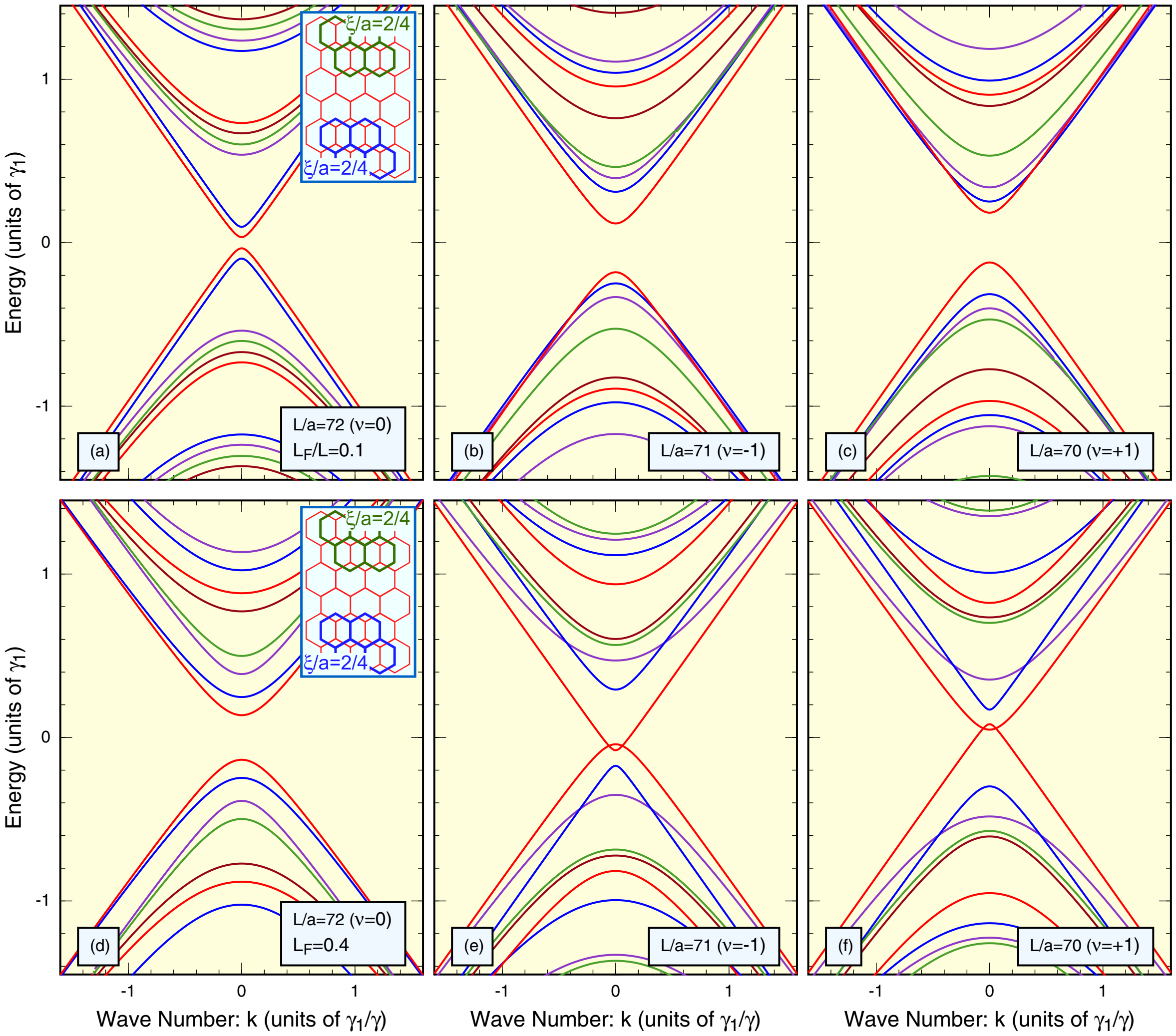

FIG. 15. Calculated band structure of collapsed nanotubes with $\xi/a = \frac{1}{2}$ having zigzag structures. (a) $(L_F/L, \nu) = (0.1, 0)$. (b) $(0.1, -1)$. (c) $(0.1, +1)$. (d) $(0.4, 0)$. (e) $(0.4, -1)$. (f) $(0.4, +1)$.

twisted stackings are reported to be present in bilayer graphene with closed edges and the displacement may be changed by annealing [101,102]. The band-structure change by sliding in bilayer graphene may be observed experimentally by scanning transmission spectroscopy or other techniques, although no experiments have been reported yet.

We have performed a systematic study of electronic states in collapsed nonchiral nanotubes such as armchair and zigzag within an effective-mass scheme, regarding them as bilayer ribbons with closed edges. Boundary conditions at closed edges, describing the connection of the envelope wave functions between the bottom and top layers, have been derived. Among electronic states in bilayers, which change sensitively depending on the relative displacement of two layers, those having wave functions matching well with the obtained boundary conditions constitute important states near the Fermi level in collapsed nanotubes.

In fact, a perfect matching or mismatching of the wave functions can occur at the closed edges for special states such as those with linear dispersion and those corresponding to band extrema near the Fermi level. Typical examples include the appearance and disappearance of k-linear bands in armchair tubes with AA stacking or half-period structure in the flattened region, and in metallic zigzag tubes with AA stacking. The lowering of the valence-band top in contrast to no influence on the conduction-band bottom in the armchair tube with AB stacking is another example.

ACKNOWLEDGMENTS

This work has been supported in part by MEXT Grants-in-Aid for Scientific Research on Innovative Areas "Science of Atomic Layers" (JPSJ KAKENHI Grants No. JP2506, No. JP26107534, and No. JP16H00925) and Scientific Research (JPSJ KAKENHI Grants No. JP24540339 and No. JP16K05412) in Japan.

APPENDIX A: TIME-REVERSAL SYMMETRY

Under the time-reversal operation T, the amplitudes $\psi_{Aj}(\boldsymbol{R})$ and $\psi_{Bj}(\boldsymbol{R})$ become their complex conjugate, $e^{-i\lambda'}\psi_{Aj}(\boldsymbol{R})^*$ and $e^{-i\lambda'}\psi_{Bj}(\boldsymbol{R})^*$, respectively, with arbitrary phase λ'. Because of the invariance under T, the amplitudes $e^{-i\lambda'}\psi_{Aj}(\boldsymbol{R})^*$ and $e^{-i\lambda'}\psi_{Bj}(\boldsymbol{R})^*$ can be written as Eqs. (5)

and (6) with F^K_{Aj}, etc., being replaced with F^{KT}_{Aj}, etc. Note that $e^{-i\boldsymbol{K}\cdot\mathbf{R}} \propto e^{i\boldsymbol{K}'\cdot\mathbf{R}}$ and $e^{-i\boldsymbol{K}'\cdot\mathbf{R}} \propto e^{i\boldsymbol{K}\cdot\mathbf{R}}$ with appropriate phase factors dependent on $\boldsymbol{R}$ [see Fig. 2(b)]. Explicitly, we have

$$\begin{pmatrix} \boldsymbol{F}^{KT}_1 \\ \boldsymbol{F}^{KT}_2 \end{pmatrix} = e^{i\lambda} \begin{pmatrix} e^{-2i\chi_1}\sigma_z & 0 \\ 0 & e^{-2i\chi_2 - i\varphi(\boldsymbol{\xi})}\sigma_z \end{pmatrix} \begin{pmatrix} \boldsymbol{F}^{K'*}_1 \\ \boldsymbol{F}^{K'*}_2 \end{pmatrix} \tag{A1}$$

in the displaced bilayer region, with $\varphi(\boldsymbol{\xi}) = (\boldsymbol{K} + \boldsymbol{K}')\cdot\boldsymbol{\xi}$ and $\lambda = \lambda' - \eta - (2\pi/3)$.

Obviously, F^{KT}_{Aj}, etc., should satisfy the Schrödinger equation same as F^K_{Aj}, etc. Let us define the Hamiltonian for the K point by

$$\mathcal{H}^K = \begin{pmatrix} \mathcal{H}_{11} & \mathcal{H}_{12} \\ \mathcal{H}_{21} & \mathcal{H}_{22} \end{pmatrix}. \tag{A2}$$

Then, Eq. (A1) gives the corresponding Hamiltonian for the K' point:

$$\begin{aligned} \mathcal{H}^{K'} &= \begin{pmatrix} e^{-2i\chi_1}\sigma_z & 0 \\ 0 & e^{-2i\chi_2 - i\varphi(\boldsymbol{\xi})}\sigma_z \end{pmatrix} \begin{pmatrix} \mathcal{H}^*_{11} & \mathcal{H}^*_{12} \\ \mathcal{H}^*_{21} & \mathcal{H}^*_{22} \end{pmatrix} \\ &\quad \times \begin{pmatrix} e^{+2i\chi_1}\sigma_z & 0 \\ 0 & e^{+2i\chi_2 + i\varphi(\boldsymbol{\xi})}\sigma_z \end{pmatrix} \\ &= \begin{pmatrix} \sigma_z\mathcal{H}^*_{11}\sigma_z & \sigma_z\mathcal{H}^*_{12}\sigma_z e^{-2i\chi_{12} + i\varphi(\boldsymbol{\xi})} \\ \sigma_z\mathcal{H}^*_{21}\sigma_z e^{+2i\chi_{12} - i\varphi(\boldsymbol{\xi})} & \sigma_z\mathcal{H}^*_{22}\sigma_z \end{pmatrix}. \end{aligned} \tag{A3}$$

This gives $\sigma_x\mathcal{H}^*_{11}\sigma_z = \gamma(\boldsymbol{\sigma}^*\cdot\hat{\boldsymbol{k}})$ for $\mathcal{H}_{11} = \gamma(\boldsymbol{\sigma}\cdot\hat{\boldsymbol{k}})$ and the same for $\mathcal{H}_{22}$. It is quite natural that only the interlayer components of the Hamiltonian are affected by relative phase χ_{12} and displacement $\boldsymbol{\xi}$ under the time reversal.

APPENDIX B: ELECTRON REFLECTION BY CLOSED EDGES

1. Transfer matrix in monolayer region

First, we consider the transfer matrix in a monolayer region. For given energy ε and wave vector k_y satisfying $|k_y| \leqslant |\varepsilon|/\gamma$, we have

$$U^K(x) = \frac{1}{\cos\theta_M} \begin{pmatrix} \cos(\theta_M - k^M_x x) & is_M \sin(k^M_x x) \\ is_M \sin(k^M_x x) & \cos(\theta_M + k^M_x x) \end{pmatrix}, \tag{B1}$$

$$U^{K'}(x) = \frac{1}{\cos\theta_M} \begin{pmatrix} \cos(\theta_M + k^M_x x) & is_M \sin(k^M_x x) \\ is_M \sin(k^M_x x) & \cos(\theta_M - k^M_x x) \end{pmatrix}, \tag{B2}$$

with

$$s_M \equiv \mathrm{sgn}(\varepsilon), \quad \sin\theta_M \equiv \frac{\gamma k_y}{|\varepsilon|}, \quad k^M_x \equiv \sqrt{\frac{\varepsilon^2}{\gamma^2} - k_y^2}. \tag{B3}$$

In the case $|k_y| > |\varepsilon|/\gamma$, only evanescent states are present and the transfer matrix is given by

$$\begin{aligned} U^K(x) &= \frac{1}{\sinh\theta_M} \\ &\quad \times \begin{pmatrix} \sinh(\theta_M + s_y\kappa^M_x x) & is_M \sinh(\kappa^M_x x) \\ is_M \sinh(\kappa^M_x x) & \sinh(\theta_M - s_y\kappa^M_x x) \end{pmatrix}, \end{aligned} \tag{B4}$$

$$\begin{aligned} U^{K'}(x) &= \frac{1}{\sinh\theta_M} \\ &\quad \times \begin{pmatrix} \sinh(\theta_M - s_y\kappa^M_x x) & is_M \sinh(\kappa^M_x x) \\ is_M \sinh(\kappa^M_x x) & \sinh(\theta_M + s_y\kappa^M_x x) \end{pmatrix}, \end{aligned} \tag{B5}$$

with

$$s_y \equiv \mathrm{sgn}(k_y), \quad \cosh\theta_M \equiv \frac{\gamma|k_y|}{|\varepsilon|}, \quad \kappa^M_x \equiv \sqrt{k_y^2 - \frac{\varepsilon^2}{\gamma^2}}. \tag{B6}$$

The transfer matrices satisfy

$$\det U^K = \det U^{K'} = 1, \tag{B7}$$

$$\sigma_z U^K(\varepsilon)\sigma_z = U^K(-\varepsilon), \tag{B8}$$

$$\sigma_z U^{K'}(\varepsilon)\sigma_z = U^{K'}(-\varepsilon). \tag{B9}$$

The last two of the above give the symmetry under energy inversion in some collapsed nanotubes, as will be shown in the following.

2. Armchair displacement: *AA* stacking

In armchair nanotubes, the energy bands associated with the K' point are related to those with the K point through $\varepsilon_{K'}(k) = \varepsilon_K(-k)$, and therefore we shall confine ourselves to those with the K point in the following. When a collapsed armchair nanotube has an AA stacking structure with $\xi = 0$ in the flattened bilayer region, for which $u = \gamma_1$ and $v = w = 0$, the Hamiltonian becomes

$$\mathcal{H}_K = \begin{pmatrix} \gamma(\boldsymbol{\sigma}\cdot\hat{\boldsymbol{k}}) & \gamma_1\sigma_0 \\ \gamma_1\sigma_0 & \gamma(\boldsymbol{\sigma}\cdot\hat{\boldsymbol{k}}) \end{pmatrix}, \tag{B10}$$

where we have chosen $\chi = 0$ [see Eqs. (15), (20), and (66) and Fig. 5]. Then, the boundary conditions are

$$\boldsymbol{F}^K_{1k}(x_L) = \sigma_y U^K_L \boldsymbol{F}^K_{2k}(x_L), \tag{B11}$$

$$\boldsymbol{F}^K_{1k}(x_R) = \sigma_y U^K_R \boldsymbol{F}^K_{2k}(x_R). \tag{B12}$$

Under unitary transformation

$$\tilde{\boldsymbol{F}}^K = U\boldsymbol{F}^K, \tag{B13}$$

with

$$U = \begin{pmatrix} \sigma_z & 0 \\ 0 & -\sigma_z \end{pmatrix}, \tag{B14}$$

the Hamiltonian is transformed into

$$\tilde{\mathcal{H}}_K = U\mathcal{H}_K U^\dagger = -\mathcal{H}_K. \tag{B15}$$

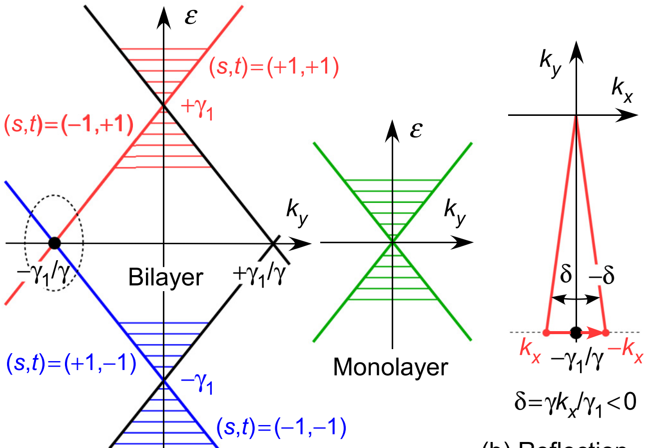

(a) Energy Bands

(b) Reflection (Right Edge)

FIG. 16. (a) Schematic illustration of energy bands in an AA-stacked bilayer graphene and in monolayer graphene. The region in the vicinity of $k_x=0$ and $k_y=-\gamma_1/\gamma$ is denoted by a dotted ellipse. (b) A reflection process at the right boundary for the band $(s,t)=(-1,+1)$, denoted by a (red) solid line in (a).

Further, the boundary conditions are transformed into

$$\tilde{\boldsymbol{F}}^K_{1k}(x_L)=\sigma_y U^K_L(-\varepsilon)\tilde{\boldsymbol{F}}^K_{2k}(x_L), \tag{B16}$$

$$\tilde{\boldsymbol{F}}^K_{1k}(x_R)=\sigma_y U^K_R(-\varepsilon)\tilde{\boldsymbol{F}}^K_{2k}(x_R). \tag{B17}$$

The above results show that the energy bands are symmetric under energy inversion $\varepsilon\leftrightarrow-\varepsilon$.

The energy bands and the corresponding wave functions in the bilayer region become

$$\varepsilon_{st}(k)=s\gamma k+t\gamma_1, \tag{B18}$$

$$\boldsymbol{F}_{stk}(\boldsymbol{r})=\frac{1}{2}\begin{pmatrix}1\\ se^{i\theta}\\ t\\ ste^{i\theta}\end{pmatrix}\exp(i\boldsymbol{k}\cdot\boldsymbol{r}), \tag{B19}$$

with $s=\pm1$, $t=\pm1$, $k=\sqrt{k_x^2+k_y^2}$, $k_x=k\cos\theta$, and $k_y=k\sin\theta$. Let us consider the bands in the vicinity of $k_y=-\gamma_1/\gamma$, $\varepsilon\approx0$, and $k_x=0$, in particular, $(s,t)=(-1,+1)$ as illustrated in Fig. 16 [the region surrounded by a dotted ellipse in (a)]. As illustrated in Fig. 16(b), the incident wave has $k_x<0$ and the reflected wave has $-k_x>0$ at the right boundary $x=x_R$. The wave function is written as

$$\boldsymbol{F}_R(\boldsymbol{r})=\begin{pmatrix}1\\ i\ {}^{+i\delta}\\ 1\\ i\ e^{+i\delta}\end{pmatrix}e^{+ik_xx_R+ik_yy}$$

$$+r_R\begin{pmatrix}1\\ i\ e^{-i\delta}\\ 1\\ i\ e^{-i\delta}\end{pmatrix}e^{-ik_xx_R+ik_yy}, \tag{B20}$$

apart from normalization, where r_R is the reflection coefficient and

$$\delta\equiv\frac{\gamma k_x}{\gamma_1}<0. \tag{B21}$$

For this state, only evanescent states are present in the monolayer region, and we have $s_y=-1$, $\cosh\theta_M\approx\sinh\theta_M\gg1$, $\kappa_x^M\approx\gamma_1/\gamma$, $k_y\sim-(\gamma_1/\gamma)$. Let us further consider the case of small $L_R\ll\gamma/\gamma_1$. The transfer matrix is approximated by

$$U_R\approx\begin{pmatrix}e^{-\gamma_1L_R/\gamma} & 0\\ 0 & e^{+\gamma_1L_R/\gamma}\end{pmatrix}. \tag{B22}$$

Then, the boundary conditions in Eq. (B12) become

$$\begin{pmatrix}1\\ i\ e^{+i\delta}\end{pmatrix}e^{2ik_xx_R}+r_R\begin{pmatrix}1\\ i\ e^{-i\delta}\end{pmatrix}$$

$$=\begin{pmatrix}e^{\gamma_1L_R/\gamma}e^{i\delta}\\ i\ e^{-\gamma_1L_R/\gamma}\end{pmatrix}e^{2ik_xx_R}+r_R\begin{pmatrix}e^{\gamma_1L_R/\gamma}e^{-i\delta}\\ i\ e^{-\gamma_1L_R/\gamma}\end{pmatrix}. \tag{B23}$$

These two equations are satisfied if and only if

$$r_R=\frac{e^{+\gamma_1L_R/\gamma}e^{+i\delta}-1}{1-e^{+\gamma_1L_R/\gamma}e^{-i\delta}}e^{+2ik_xx_R}. \tag{B24}$$

The fact that the reflection coefficient is uniquely determined from a set of two equations justify that reflection does not take place into other bands with $t=-1$. For $\gamma_1L_R/\gamma\ll|\delta|\ll1$, in particular, we have

$$r_R\approx\exp\left(i\frac{\gamma k_x}{\gamma_1}-i\frac{2\gamma_1^2L_R}{\gamma^2k_x}\right)e^{2ik_xx_R}. \tag{B25}$$

At the left boundary, similarly, the reflection coefficient becomes

$$r_L\approx\exp\left(-i\frac{\gamma k_x}{\gamma_1}-i\frac{2\gamma_1^2L_L}{\gamma^2k_x}\right)e^{-2ik_xx_L}. \tag{B26}$$

The energy bands are given by the condition $r_Lr_R=1$ or

$$k_xL_F-2\frac{\gamma_1^2}{\gamma^2k_x}L_C=2\pi j, \tag{B27}$$

with integer j, where we have used $x_R-x_L=L_F/2$ and $L_R+L_L=L_C$. For the linear band corresponding to $j=0$, we have

$$\gamma k_x=-\gamma_1\sqrt{\frac{2L_C}{L_F}}, \tag{B28}$$

where we have used the fact that $k_x<0$. Correspondingly, with k_y being replaced with k of the collapsed nanotube, the energy levels become

$$\varepsilon=-\gamma\sqrt{k_x^2+k^2}+\gamma_1\approx-\gamma|k|+\gamma_1\left(1-\frac{L_C}{L_F}\right). \tag{B29}$$

This shows that the linear band given by $\varepsilon=+\gamma k+\gamma_1$ is shifted to the positive k direction by the amount proportional to

L_C/L_F with the increase of the width of the curved monolayer region. Because of the symmetry under energy inversion, the completely same behavior is obtained for the band $(s,t) = (+1,-1)$.

For the band $(s,t) = (-1,+1)$ in the vicinity of $k_y = +\gamma_1/\gamma$ and $\varepsilon \approx 0$, the incident wave has $k_x < 0$ and the reflected wave has $-k_x > 0$ at the right boundary. The wave function at the right boundary is written as

$$\boldsymbol{F}_R(\boldsymbol{r}) = \begin{pmatrix} 1 \\ -i\,e^{-i\delta} \\ 1 \\ -i\,e^{-i\delta} \end{pmatrix} e^{+ik_x x_R + ik_y y} + r_R \begin{pmatrix} 1 \\ -i\,e^{+i\delta} \\ 1 \\ -i\,e^{+i\delta} \end{pmatrix} e^{-ik_x x_R + ik_y y}, \tag{B30}$$

apart from normalization. In a similar manner, we have

$$r_R \approx -e^{-i\delta} e^{+2ik_x x_R},$$
$$r_L \approx -e^{+i\delta} e^{-2ik_x x_L}. \tag{B31}$$

These results show that the wave function should vanish in the vicinity of both right and left boundaries. Therefore, states with $k_x \approx 0$ having a near-linear band are not allowed in the collapsed nanotube. The quantization condition $r_L r_R = 1$ gives

$$k_x = \frac{2\pi j}{L_F}, \tag{B32}$$

with integer j, where $j = 0$ is not allowed. Because of the symmetry under energy inversion, the completely same behavior is obtained for the band $(s,t) = (+1,-1)$. Figure 6(a) schematically shows remaining linear bands for $L_C/L \ll 1$.

3. Armchair displacement: *AB* stacking

Let us consider the case of $\xi/(\sqrt{3}a) = \frac{1}{3}$, for which $u = v = 0$ and $w = \gamma_1$. The effective Hamiltonian is given by Eq. (69). The eigenenergies are given by

$$\varepsilon_{st}(k) = \begin{cases} 2s\,\varepsilon(k)\sin^2(\psi/2) & (t = +1); \\ 2s\,\varepsilon(k)\cos^2(\psi/2) & (t = -1), \end{cases} \tag{B33}$$

where the conduction bands are denoted by $s = +1$, the valence bands by $s = -1$, the bands touching at $\varepsilon = 0$ by $t = +1$, those split in energy by $\pm\gamma_1$ by $t = -1$, and

$$\varepsilon(k) = \sqrt{\left(\frac{\gamma_1}{2}\right)^2 + (\gamma k)^2}, \quad \tan\psi = \frac{2\gamma k}{\gamma_1}. \tag{B34}$$

The corresponding wave functions are given by

$$\boldsymbol{F}_{s,+1} = \begin{pmatrix} s\cos(\psi/2) \\ e^{i\theta}\sin(\psi/2) \\ -i\,s\,e^{i\theta}\sin(\psi/2) \\ -i\,e^{2i\theta}\cos(\psi/2) \end{pmatrix} e^{i\boldsymbol{k}\cdot\boldsymbol{r}}, \tag{B35}$$

$$\boldsymbol{F}_{s,-1} = \begin{pmatrix} s\sin(\psi/2) \\ e^{i\theta}\cos(\psi/2) \\ i\,s\,e^{i\theta}\cos(\psi/2) \\ i\,e^{2i\theta}\sin(\psi/2) \end{pmatrix} e^{i\boldsymbol{k}\cdot\boldsymbol{r}}, \tag{B36}$$

with $\theta = \tan^{-1}(k_y/k_x)$. In the vicinity of zero energy, $\psi \approx 2\gamma k/\gamma_1$ and $\varepsilon_{s,+1}(k) \approx s\gamma^2 k^2/\gamma_1$.

Let us consider the case $|k_x| \ll |k_y| \ll \gamma_1/\gamma$ for the purpose of determining whether the band touching $\varepsilon = 0$ survives in the presence of closed edges. In the monolayer region, because $|\varepsilon| \ll \gamma|k_y|$, only evanescent waves are present and therefore $\kappa_x^M \approx |k_y|$ and $\theta_M \gg 1$. Noting $s_M = s$, we have

$$U_R \approx \begin{pmatrix} e^{+k_y L_R} & 0 \\ 0 & e^{-k_y L_R} \end{pmatrix}, \quad U_L \approx \begin{pmatrix} e^{-k_y L_L} & 0 \\ 0 & e^{+k_y L_L} \end{pmatrix}. \tag{B37}$$

At the right edge, the incident wave has $\theta = (\pi/2) + \delta$ and the reflected wave $\theta = (\pi/2) - \delta$ with $\delta \ll 1$ for $k_y > 0$. Therefore, the wave function is written as

$$\boldsymbol{F}^R_{s,+1}(\boldsymbol{r}) = \begin{pmatrix} s\cos(\psi/2) \\ i\,e^{i\delta}\sin(\psi/2) \\ s\,e^{i\delta}\sin(\psi/2) \\ i\,e^{2i\delta}\cos(\psi/2) \end{pmatrix} e^{ik_x x_R + ik_y y} + r_R \begin{pmatrix} s\cos(\psi/2) \\ i\,e^{-i\delta}\sin(\psi/2) \\ s\,e^{-i\delta}\sin(\psi/2) \\ i\,e^{-2i\delta}\cos(\psi/2) \end{pmatrix} e^{-ik_x x_R + ik_y y}, \tag{B38}$$

with reflection coefficient r_R. The boundary conditions in Eq. (B12) give

$$\begin{pmatrix} s\cos(\psi/2) \\ i\,e^{i\delta}\sin(\psi/2) \end{pmatrix} e^{2ik_x x_R} + r_R \begin{pmatrix} s\cos(\psi/2) \\ i\,e^{-i\delta}\sin(\psi/2) \end{pmatrix}$$
$$= \begin{pmatrix} e^{-k_y L_R} e^{+2i\delta}\cos(\psi/2) \\ i\,s\,e^{+k_y L_R} e^{+i\delta}\sin(\psi/2) \end{pmatrix} e^{2ik_x x_R} + r_R \begin{pmatrix} e^{-k_y L_R} e^{-2i\delta}\cos(\psi/2) \\ i\,s\,e^{+k_y L_R} e^{-i\delta}\sin(\psi/2) \end{pmatrix}. \tag{B39}$$

Only the first equation is important and gives

$$r_R = -\frac{s - e^{-k_y L_R} e^{+2i\delta}}{s - e^{-k_y L_R} e^{-2i\delta}}. \tag{B40}$$

In the limit $\varepsilon \to 0$, we have $r_R = s\,e^{2i\delta}$, which becomes, in the limit of $\delta \to 0$, $r_R = +1$ for $s = +1$ and $r_R = -1$ for $s = -1$. The same result is obtained at the left edge. This shows that a near-parabolic band touching zero energy survives for the conduction band with $r_R \approx +1$, but does not for the valence band with $r_R \approx -1$.

For $k_x \approx 0$, the wave functions become $F^{A1}_{s,+1} \approx s$, $F^{B1}_{s,+1} \approx F^{B1}_{s,+1} \approx 0$, and $F^{B2}_{s,+1} \approx i$, apart from normalization. According to Eqs. (5) and (6), the corresponding amplitudes in the tight-binding model become

$$\psi_{A1}[\boldsymbol{R}_{B1}+l_R(2\boldsymbol{a}+\boldsymbol{b})+\boldsymbol{\tau}_2] = s\omega^{-1}e^{i\chi_1}e^{i\boldsymbol{K}\cdot\boldsymbol{R}_{B1}}, \tag{B41}$$

$$\psi_{B2}[\boldsymbol{R}_{B1}+\boldsymbol{\xi}] = -\omega^{-1}e^{i\chi_1}e^{i\boldsymbol{K}\cdot\boldsymbol{R}_{B1}}, \tag{B42}$$

and $\psi_{B1}\approx\psi_{A2}\approx 0$, where we have used Eqs. (15) and (20). This shows that the boundary condition (26) is satisfied for $s=+1$ but not for $s=-1$. Namely, the wave functions are smoothly connected between the top and bottom layers through the curved monolayer region for the conduction band, but not for the valence band. This is the reason for the lowering of the valence band top, resulting in the band-gap opening.

To see bands away from zero energy, we next consider the case $k_y=0$ for the band $t=+1$. We have $\theta_M=0$ and

$$U_R^K = \begin{pmatrix} \cos(k_x^M L_R) & i\,s\sin(k_x^M L_R) \\ i\,s\sin(k_x^M L_R) & \cos(k_x^M L_R) \end{pmatrix}. \tag{B43}$$

At the right edge, the incident wave has $k_x>0$ for $s=+1$ and $k_x<0$ for $s=-1$. Therefore, the wave function is written as

$$\boldsymbol{F}^R_{s,+1}(\boldsymbol{r}) = \begin{pmatrix} s\cos(\psi/2) \\ s\sin(\psi/2) \\ -i\sin(\psi/2) \\ -i\cos(\psi/2) \end{pmatrix} e^{+ik_xx_R} + r_R \begin{pmatrix} s\cos(\psi/2) \\ -s\sin(\psi/2) \\ +i\sin(\psi/2) \\ -i\cos(\psi/2) \end{pmatrix} e^{-ik_xx_R}. \tag{B44}$$

After some manipulations, the boundary conditions (B12) give

$$r_R = -s\frac{\sin\psi - i\sin(k_x^M L_R)\cos\psi}{\cos(k_x^M L_R)\sin\psi - i\,s\sin(k_x^M L_R)}e^{+2i\,k_xx_R}. \tag{B45}$$

In the energy region close to zero energy, we have $\psi\approx 2\gamma k_x/\gamma_1\ll 1$ and $k_x^M\approx\gamma k_x^2/\gamma_1$. Then, we have

$$r_R = -s\,e^{i(1-s)k_xL_R/2}e^{+2ik_xx_R}. \tag{B46}$$

Similarly, at the left edge, we have

$$r_L = -s\,e^{i(1-s)k_xL_L/2}e^{-2ik_xx_L}. \tag{B47}$$

The quantization condition $r_Rr_L=1$ gives

$$\left(L_F+\frac{1-s}{2}L_C\right)k_x = 2\pi j, \tag{B48}$$

giving $k_x=2\pi j/L_F$ for $s=+1$ and $k_x=2\pi j/L$ for $s=-1$, with integer j. This shows that the valence band is quantized into

$$\varepsilon_j = -\sqrt{\left(\frac{\gamma_1}{2}\right)^2+\gamma^2\left(\frac{2\pi j}{L}\right)^2}+\frac{\gamma_1}{2}\quad(j=1,2,\dots), \tag{B49}$$

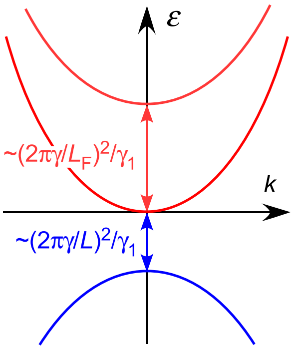

FIG. 17. A schematic illustration of low-lying bands in a collapsed armchair nanotube with AB stacking structure in the flattened region.

and the conduction band is

$$\varepsilon_j = +\sqrt{\left(\frac{\gamma_1}{2}\right)^2+\gamma^2\left(\frac{2\pi j}{L_F}\right)^2}-\frac{\gamma_1}{2}\quad(j=0,1,\dots). \tag{B50}$$

These results are schematically illustrated in Fig. 17 for the case $2\pi\gamma/L\ll\gamma_1$, which explains the features of the bands located near zero energy in Fig. 11(d).

In the energy region corresponding to the excited conduction and valence bands with $t=-1$, the curved monolayer region has a large density of states and its effect cannot be neglected for realistic L_L and L_R. Therefore, similar analysis limited to small L_L and L_R is not so meaningful. Numerical results in Fig. 11(d) show that clear "edge" states localized in the monolayer region appear above the top of the lower valence band in addition to bands associated with the excited conduction and valence bands in the bilayer region. These edge states are given by the (red) dotted line and the (green) solid line having their maxima around $\varepsilon/\gamma_1=-0.7$ and -0.8. These bands are nearly degenerate for sufficiently large L_F, but split into bonding and antibonding states for small L_F.

4. Armchair displacement: Tilted Weyl cones

Let us consider the case $0<\xi/(\sqrt{3}a)<\frac{1}{3}$ in a collapsed armchair nanotube. The Hamiltonian for the K point is given by Eq. (76). For $k_y\approx 0$, the transfer matrix in the monolayer region is given by $U_R\approx U_L\approx 1$. The reflection at a closed edge occurs only between different cones, i.e., from $+k_0$ to $-k_0$ and from $-k_0$ to $+k_0$. The reflection coefficients are calculated using the wave functions (72)–(75) and the boundary conditions (B11) and (B12). The coefficient for reflection from $+(k_0+k_x)$ to $-(k_0+k_x)$ at the right edge and that from $-(k_0+k_x)$ to $+(k_0+k_x)$ at the left edge are given by

$$\begin{aligned} r^R_{-+} &= +i\,e^{+2i\,(k_0+k_x)x_R}, \\ r^L_{+-} &= -i\,e^{-2i\,(k_0+k_x)x_L}, \end{aligned} \tag{B51}$$

where k_x is measured from $+k_0$. The allowed bands are determined by $r^R_{-+}r^L_{+-}=1$, giving

$$(k_x+k_0)L_F = 2\pi j\quad(j=1,2,\dots). \tag{B52}$$

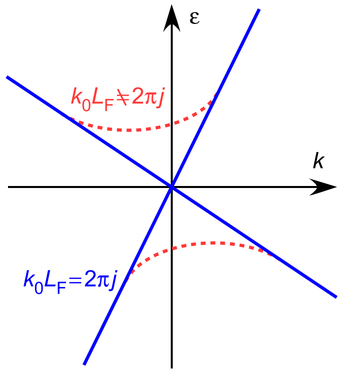

FIG. 18. A schematic illustration of the energy band appearing due to interferences between two tilted Weyl cones. $0 < \xi/(\sqrt{3}a) < \frac{1}{3}$.

The energy bands in the collapsed nanotube become

$$\varepsilon_j(k) = \pm\sqrt{\alpha_x^2 k_j^2 + \alpha_y^2 k^2} + \beta k, \tag{B53}$$

with $k_j = (2\pi j/L_F) - k_0$. This shows that linearly crossing bands given by Eq. (87) appear when $k_0 L_F = 2\pi j$. The dispersion is illustrated in Fig. 18. The band parameters are shown in Fig. 8.

5. Zigzag displacement: *AA* stacking

Let us consider the case $\xi = 0$ in a collapsed zigzag nanotube. The Hamiltonian $\mathcal{H}_K$ for the K point is given by Eq. (B10) and $\mathcal{H}_{K'}$ for the K' point is obtained from Eq. (B10) by replacing $\boldsymbol{\sigma}$ with $\boldsymbol{\sigma}^*$, if we choose $\chi_{12} = 0$, giving $\chi' = \chi'' = 0$ [see Eq. (40)]. The corresponding energy bands are illustrated together with those in the monolayer region in Fig. 19. The boundary conditions become

$$\begin{aligned}
\boldsymbol{F}_{2k}^{K}(x_R) &= -\omega^{+n_R}\sigma_z U_R^{K'} \boldsymbol{F}_{1k}^{K'}(x_R),\\
\boldsymbol{F}_{2k}^{K'}(x_R) &= -\omega^{-n_R}\sigma_z U_R^{K} \boldsymbol{F}_{1k}^{K}(x_R),\\
\boldsymbol{F}_{2k}^{K}(x_L) &= -\omega^{+n_L}\sigma_z U_L^{K'} \boldsymbol{F}_{1k}^{K'}(x_L),\\
\boldsymbol{F}_{2k}^{K'}(x_L) &= -\omega^{-n_L}\sigma_z U_L^{K} \boldsymbol{F}_{1k}^{K}(x_L).
\end{aligned} \tag{B54}$$

In terms of unitary transformations

$$\tilde{\boldsymbol{F}}_K = U_K \boldsymbol{F}_K, \quad \tilde{\boldsymbol{F}}_{K'} = U_{K'} \boldsymbol{F}_{K'}, \tag{B55}$$

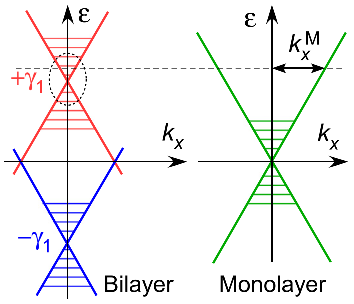

FIG. 19. Energy versus wave vector in the *AA* stacked bilayer graphene and the monolayer graphene. The region which we are interested in is denoted by a dotted ellipse.

with

$$U_K = \begin{pmatrix} +\sigma_z & 0 \\ 0 & -\sigma_z \end{pmatrix}, \quad U_{K'} = \begin{pmatrix} -\sigma_z & 0 \\ 0 & +\sigma_z \end{pmatrix}, \tag{B56}$$

the Hamiltonians are transformed into

$$\begin{aligned}
\tilde{\mathcal{H}}_K &= U_K \mathcal{H}_K U_K^\dagger = -\mathcal{H}_K,\\
\tilde{\mathcal{H}}_K &= U_{K'} \mathcal{H}_{K'} U_{K'}^\dagger = -\mathcal{H}_{K'}.
\end{aligned} \tag{B57}$$

The boundary conditions are transformed into

$$\begin{aligned}
\tilde{\boldsymbol{F}}_{2k}^{K}(x_R) &= -\omega^{+n_R}\sigma_z U_R^{K'}(-\varepsilon) \tilde{\boldsymbol{F}}_{1k}^{K'}(x_R),\\
\tilde{\boldsymbol{F}}_{2k}^{K'}(x_R) &= -\omega^{-n_R}\sigma_z U_R^{K}(-\varepsilon) \tilde{\boldsymbol{F}}_{1k}^{K}(x_R),\\
\tilde{\boldsymbol{F}}_{2k}^{K}(x_L) &= -\omega^{+n_L}\sigma_z U_L^{K'}(-\varepsilon) \tilde{\boldsymbol{F}}_{1k}^{K'}(x_L),\\
\tilde{\boldsymbol{F}}_{2k}^{K'}(x_L) &= -\omega^{-n_L}\sigma_z U_L^{K}(-\varepsilon) \tilde{\boldsymbol{F}}_{1k}^{K}(x_L).
\end{aligned} \tag{B58}$$

The above results show that the energy bands are symmetric under energy inversion $\varepsilon \leftrightarrow -\varepsilon$. Further, the energy bands with $t = +1$ and -1 do not couple at the right and left closed edges as will be clear in the following. In general, reflection coefficients become (2,2) matrices, i.e.,

$$\hat{r}_R = \begin{pmatrix} r_{KK}^R & r_{KK'}^R \\ r_{K'K}^R & r_{K'K'}^R \end{pmatrix}, \quad \hat{r}_L = \begin{pmatrix} r_{KK}^L & r_{KK'}^L \\ r_{K'K}^L & r_{K'K'}^L \end{pmatrix}. \tag{B59}$$

We shall consider small k_y and the energy region $\varepsilon \approx \gamma_1$ close to the upper Weyl cone $t = +1$, having $\varepsilon_s(\boldsymbol{k}) = s\gamma|\boldsymbol{k}| + \gamma_1$, in the following. This region is surrounded by a dotted ellipse in Fig. 19. The wave functions are

$$\boldsymbol{F}_s^K(\boldsymbol{r}) = \begin{pmatrix} 1 \\ se^{i\theta} \\ 1 \\ se^{i\theta} \end{pmatrix} e^{i\boldsymbol{k}\cdot\boldsymbol{r}}, \quad \boldsymbol{F}_s^{K'}(\boldsymbol{r}) = \begin{pmatrix} 1 \\ se^{-i\theta} \\ 1 \\ se^{-i\theta} \end{pmatrix} e^{i\boldsymbol{k}\cdot\boldsymbol{r}}. \tag{B60}$$

For an incident wave associated with the K point at the right edge, reflected waves can be at the K and K' points. The wave vector of the incident wave has $k_x > 0$ for $\varepsilon > +\gamma_1$ and $k_x < 0$ for $\varepsilon < +\gamma_1$. The wave function for the K point and that for the K' point are written as

$$\boldsymbol{F}_{sK}^R(\boldsymbol{r}) = \begin{pmatrix} 1 \\ se^{i\theta} \\ 1 \\ se^{i\theta} \end{pmatrix} e^{ik_x x_R + ik_y y} + r_{KK}^R \begin{pmatrix} 1 \\ -se^{-i\theta} \\ 1 \\ -se^{-i\theta} \end{pmatrix} e^{-ik_x x_R + ik_y y}, \tag{B61}$$

$$\boldsymbol{F}_{sK'}^R(\boldsymbol{r}) = r_{K'K}^R \begin{pmatrix} 1 \\ -se^{+i\theta} \\ 1 \\ -se^{+i\theta} \end{pmatrix} e^{-ik_x x_R + ik_y y}, \tag{B62}$$

with reflection coefficients $r_{K'K}^R$ and r_{KK}^R.

The boundary conditions (B54) give

$$r^R_{K'K}\begin{pmatrix}1\\ -e^{i\theta}\end{pmatrix}e^{-ik_xx_R}=-\omega^{-n_R}\sigma_zU^K_R \\ \times\left[\begin{pmatrix}1\\ e^{i\theta}\end{pmatrix}e^{ik_xx_R}+r^R_{KK}\begin{pmatrix}1\\ -e^{-i\theta}\end{pmatrix}e^{-ik_xx_R}\right]. \tag{B63}$$

In the following, we shall consider the case that $|k_y|\ll|k_x|$ or $|\theta|\ll 1$. Then, the transfer matrix can be expanded as

$$U_R=\begin{pmatrix}\cos(k^M_xL_R) & is_M\sin(k^M_xL_R)\\ is_M\sin(k^M_xL_R) & \cos(k^M_xL_R)\end{pmatrix} \\ +\theta_M\sin(k^M_xL_R)\sigma_z, \tag{B64}$$

to the first order in $\theta_M\propto k_y$, where

$$\gamma k_x+\gamma_1=s_M\gamma k^M_x. \tag{B65}$$

The reflection coefficients can be solved by expansion with respect to k_y:

$$r^R_{K'K}=r^{R(0)}_{K'K}+r^{R(1)}_{K'K},\quad r^R_{KK}=r^{R(0)}_{KK}+r^{R(1)}_{KK}, \tag{B66}$$

where $r^{R(0)}_{K'K}\propto k^0_y$, $r^{R(1)}_{K'K}\propto k_y$, etc. A straightforward calculation shows that $r^{R(0)}_{KK}=0$ and $r^{R(1)}_{K'K}=0$. The results are summarized as

$$\hat{r}_R\approx\begin{pmatrix}+\zeta(L_R) & -\omega^{+n_R}\\ -\omega^{-n_R} & -\zeta(L_R)\end{pmatrix}e^{is_Mk^M_xL_R}e^{+2ik_xx_R}, \tag{B67}$$

with

$$\zeta(x)\equiv(\theta-s_M\theta_M)\sin(s_Mk^M_xx). \tag{B68}$$

The diagonal element corresponding to the reflection into the same valley is proportional to $\zeta(L_R)\propto k_y$ and therefore is much smaller than the off-diagonal element corresponding to the reflection into the different valley. Similar calculations give

$$\hat{r}_L\approx\begin{pmatrix}-\zeta(L_L) & -\omega^{+n_L}\\ -\omega^{-n_L} & +\zeta(L_L)\end{pmatrix}e^{is_Mk^M_xL_L}e^{-2ik_xx_R}. \tag{B69}$$

Their product becomes

$$\hat{r}_L\hat{r}_R\approx e^{is_Mk^M_xL_C}e^{ik_xL_F}\begin{pmatrix}\omega^{+\nu} & \omega^{n_R}[\zeta(L_R)+\omega^\nu\zeta(L_L)]\\ -\omega^{n_R}[\zeta(L_R)+\omega^\nu\zeta(L_L)] & \omega^{-\nu}\end{pmatrix}. \tag{B70}$$

For $k_y=0$, i.e., $\theta=\theta_M=0$, off-diagonal elements identically vanish and the wave vector is quantized into

$$s_Mk^M_xL_C+k_xL_F=2\pi\left(j\pm\frac{\nu}{3}\right), \tag{B71}$$

with integer j. Using Eq. (B65), we have

$$k_x=\frac{2\pi}{L}\left(j\pm\frac{\nu}{3}\right)-\frac{\gamma_1}{\gamma}\frac{L_C}{L}. \tag{B72}$$

The quantization into integer multiple of $2\pi/L$ depending on ν is exactly the same as in cylindrical nanotubes apart from a shift proportional to L_C/L.

For nonzero but small k_y, we have the condition

$$k_y=\theta k_x=\theta_Mk^M_x. \tag{B73}$$

With the use of Eq. (B65), we have

$$\theta-s_M\theta_M=s_M\frac{\gamma_1}{\gamma}\frac{k_y}{k_xk^M_x}. \tag{B74}$$

Effects of nonzero but small k_y strongly depend on $\nu=0$ or $\nu=\pm1$. In fact, for $\nu=\pm1$ corresponding to semiconducting nanotubes, the large diagonal elements of $\hat{r}_L\hat{r}_R$ are different between the K and K' points. In this case, effects of the off-diagonal elements appear in the eigenvalues of $\hat{r}^L\hat{r}^R$ in the second order of k_y. Therefore, the quantization conditions are not affected to the first order in k_y and the energy bands exhibit a parabolic dependence on k. Explicit numerical calculations seem to show that the coefficient of the term proportional to k^2 has the sign same as s, i.e., $\propto +k^2$ for $\varepsilon>+\gamma_1$ and $\propto -k^2$ for $\varepsilon<+\gamma_1$.

In the case of metallic nanotubes with $\nu=0$, on the other hand, the diagonal elements of $\hat{r}_L\hat{r}_R$ are the same and effects of the off-diagonal elements appear in the first order in k_y. To the first order, $\hat{r}^L\hat{r}^R$ is diagonalized as

$$\hat{r}_L\hat{r}_R=e^{is_Mk^M_xL_C}e^{i\,k_xL_F}\begin{pmatrix}e^{i[\zeta(L_R)+\zeta(L_L)]} & 0\\ 0 & e^{-i[\zeta(L_R)+\zeta(L_L)]}\end{pmatrix}. \tag{B75}$$

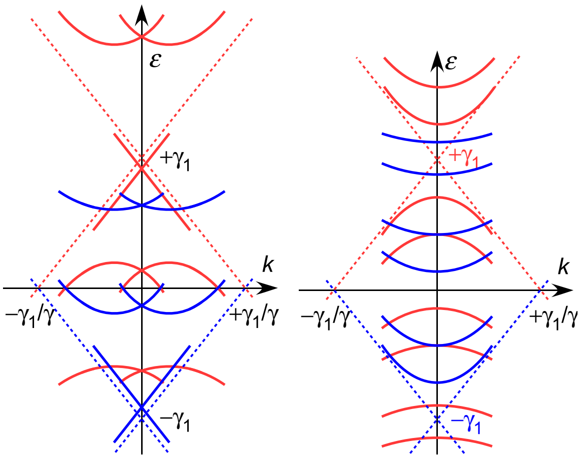

(a) ν=0 (b) ν=+1, −1

FIG. 20. A schematic illustration of the band structure of a collapsed zigzag tube having AA stacking structure in the flattened region. (a) $\nu=0$. (b) $\nu=\pm1$.

The quantization condition becomes

$$s_M k_x^M L_C + k_x L_F \pm [\zeta(L_R) + \zeta(L_L)] = 2\pi j. \tag{B76}$$

These show that the quantized wave vectors vary linearly as a function of k_y for small k_y with a coefficient dependent on the band index j. For sufficiently small L_C, we have

$$k_x \approx \begin{cases} -\frac{\gamma_1}{\gamma}\frac{L_C}{L} \pm k_y & (j = 0); \\ \frac{2\pi j}{L} - \frac{\gamma_1}{\gamma}\frac{L_C}{L} \pm \frac{\gamma_1}{\gamma}\frac{L_C}{2\pi j}k_y & (j \neq 0). \end{cases} \tag{B77}$$

The energy bands in the collapsed tube become

$$\varepsilon_j(k) = \begin{cases} -\gamma\left(\frac{\gamma_1}{\gamma}\frac{L_C}{L} \pm k\right) & (j = 0); \\ \frac{2\pi j\gamma}{L} - \gamma_1\frac{L_C}{L} \pm \frac{\gamma_1 L_C}{2\pi j}k & (j \neq 0), \end{cases} \tag{B78}$$

to the first order in k. Explicit numerical calculations seem to show again that the coefficient of the term proportional to k^2 has the sign same as s, i.e., $\propto +k^2$ for $\varepsilon > +\gamma_1$ and $\propto -k^2$ for $\varepsilon < +\gamma_1$. The energy bands for $t = -1$ can be obtained by the energy inversion. The results of the above analysis show that the band structure near $k = 0$ can be illustrated as in Fig. 20. They can explain the main features of the results of explicit numerical calculations in Sec. V [see Figs. 14(a) and 14(d)].

---

[1] S. Iijima, Nature (London) **354**, 56 (1991).

[2] S. Iijima, T. Ichihashi, and Y. Ando, Nature (London) **356**, 776 (1992).

[3] S. Iijima and T. Ichihashi, Nature (London) **363**, 603 (1993).

[4] D. S. Bethune, C. H. Kiang, M. S. de Vries, G. Gorman, R. Savoy, J. Vazquez, and R. Beyers, Nature (London) **363**, 605 (1993).

[5] N. Hamada, S. I. Sawada, and A. Oshiyama, Phys. Rev. Lett. **68**, 1579 (1992).

[6] J. W. Mintmire, B. I. Dunlap, and C. T. White, Phys. Rev. Lett. **68**, 631 (1992).

[7] R. Saito, M. Fujita, G. Dresselhaus, and M. S. Dresselhaus, Phys. Rev. B **46**, 1804 (1992).

[8] M. S. Dresselhaus, G. Dresselhaus, and R. Saito, Phys. Rev. B **45**, 6234 (1992).

[9] M. S. Dresselhaus, G. Dresselhaus, R. Saito, and P. C. Eklund, in *Elementary Excitations in Solids*, edited by J. L. Birman, C. Sebenne, and R. F. Wallis (Elsevier, Amsterdam, 1992), p. 387.

[10] R. A. Jishi, M. S. Dresselhaus, and G. Dresselhaus, Phys. Rev. B **47**, 16671 (1993).

[11] K. Tanaka, K. Okahara, M. Okada, and T. Yamabe, Chem. Phys. Lett. **191**, 469 (1992).

[12] Y. D. Gao and W. C. Herndon, Mol. Phys. **77**, 585 (1992).

[13] D. H. Robertson, D. W. Brenner, and J. W. Mintmire, Phys. Rev. B **45**, 12592 (1992).

[14] C. T. White, D. H. Robertson, and J. W. Mintmire, Phys. Rev. B **47**, 5485 (1993).

[15] H. Ajiki and T. Ando, J. Phys. Soc. Jpn. **62**, 1255 (1993).

[16] H. Ajiki and T. Ando, J. Phys. Soc. Jpn. **65**, 505 (1996).

[17] T. Ando, J. Phys. Soc. Jpn. **74**, 777 (2005) and references cited therein.

[18] N. G. Chopra, L. X. Benedict, V. H. Crespi, M. L. Cohen, S. G. Louie, and A. Zettl, Nature (London) **377**, 135 (1995).

[19] L. N. Bourgeois and L. A. Bursill, Chem. Phys. Lett. **277**, 571 (1997).

[20] L. X. Benedict, N. G. Chopra, M. L. Cohen, A. Zettl, S. G. Louie, and V. H. Crespi, Chem. Phys. Lett. **286**, 490 (1998).

[21] S. W. Liu, J. Yue, and R. J. Wehmschulte, Nano Lett. **2**, 1439 (2002).

[22] W. Z. Li, X. Yan, K. Kempa, Z. F. Ren, and M. Giersig, Carbon **45**, 2938 (2007).

[23] X. H. Zhong, R. Wang, L. B. Liu, M. Kang, Y. Y. Wen, F. Hou, J. M. Feng, and Y. L. Li, Nanotechnology **23**, 505712 (2012).

[24] H. Kohno, T. Komine, T. Hasegawa, H. Niioka, and S. Ichikawa, Nanoscale **5**, 570 (2013).

[25] C.-G. Zhang, K. Bets, S. S. Lee, Z.-Z. Sun, F. Mirri, V. L. Colvin, B. I. Yakobson, J. M. Tour, and R. H. Hauge, ACS Nano **6**, 6023 (2012).

[26] R. Martel, T. Schmidt, H. R. Shea, T. Hertel, and Ph. Avouris, Appl. Phys. Lett. **73**, 2447 (1998).

[27] T. Hertel, R. E. Walkup, and Ph. Avouris, Phys. Rev. B **58**, 13870 (1998).

[28] M. F. Yu, M. J. Dyer, and R. S. Ruoff, J. Appl. Phys. **89**, 4554 (2001).

[29] M. F. Yu, T. Kowalewski, and R. S. Ruoff, Phys. Rev. Lett. **86**, 87 (2001).

[30] C. E. Giusca, Y. Tison, and S. R. P. Silva, Phys. Rev. B **76**, 035429 (2007).

[31] C. E. Giusca, Y. Tison, and S. R. P. Silva, Nano Lett. **8**, 3350 (2008).

[32] D. H. Choi, Q. Wang, Y. Azuma, Y. Majima, J. H. Warner, Y. Miyata, H. Shinohara, and R. Kitaura, Sci. Rep. **3**, 1617 (2013).

[33] V. H. Crespi, N. G. Chopra, M. L. Cohen, A. Zettl, and S. G. Louie, Phys. Rev. B **54**, 5927 (1996).

[34] V. H. Crespi, N. G. Chopra, M. L. Cohen, A. Zettl, and V. Radmilovíc, Appl. Phys. Lett. **73**, 2435 (1998).

[35] J.-Q. Lu, J. Wu, W.-H. Duan, F. Liu, B.-F. Zhu, and B.-L. Gu, Phys. Rev. Lett. **90**, 156601 (2003).

[36] H. J. Liu and K.-J. Cho, Appl. Phys. Lett. **85**, 807 (2004).

[37] P. Tangney, R. B. Capaz, C. D. Spataru, M. L. Cohen, and S. G. Louie, Nano Lett. **5**, 2268 (2005).

[38] P. E. Lammert, P.-H. Zhang, and V. H. Crespi, Phys. Rev. Lett. **84**, 2453 (2000).

[39] H. Mehrez, A. Svizhenko, M. P. Anantram, M. Elstner, and T. Frauenheim, Phys. Rev. B **71**, 155421 (2005).

[40] J.-Q. Lu, J. Wu, W.-H. Duan, B.-L. Gu, and H. T. Johnson, J. Appl. Phys. **97**, 114314 (2005).

[41] T. Tang, A. Jagota, C.-Y. Hui, and N. J. Glassmaker, J. Appl. Phys. **97**, 074310 (2005).

[42] S. Zhang, R. Khare, T. Belytschko, K. J. Hsia, S. L. Mielke, and G. C. Schatz, Phys. Rev. B **73**, 075423 (2006).

[43] M. Hasegawa and K. Nishidate, Phys. Rev. B **74**, 115401 (2006).

[44] J. Xiao, B. Liu, Y. Huang, J. Zuo, K.-C. Hwang, and M.-F. Yu, Nanotechnology **18**, 395703 (2007).

[45] W.-B. Lu, T.-W. Chou, and B.-S. Kim, Phys. Rev. B **83**, 134113 (2011).

[46] Y.-H. Kim, H.-S. Sim, and K. J. Chang, Curr. Appl. Phys. **1**, 39 (2001).
[47] K. Nishidate and M. Hasegawa, Phys. Rev. B **78**, 195403 (2008).
[48] Y. V. Shtogun and L. M. Woods, Carbon **47**, 3252 (2009).
[49] M. Hasegawa and K. Nishidate, e-J. Surf. Sci. Nanotech. **7**, 541 (2009).
[50] K. Nishidate and M. Hasegawa, Phys. Rev. B **81**, 125414 (2010).
[51] O. E. Shklyaev, E. Mockensturm, and V. H. Crespi, Phys. Rev. Lett. **106**, 155501 (2011).
[52] J.-L. Kou, X.-Y. Zhou, Y.-Z. Fang, Y. Chen, H.-J. Lu, H.-Q. Ye, F.-M. Wu, and J.-T. Fan, Appl. Phys. Lett. **102**, 123902 (2013).
[53] M. Hasegawa, K. Nishidate, and N. Yoshimoto, Phys. Rev. B **92**, 245429 (2015).
[54] T. Nakanishi and T. Ando, Phys. Rev. B **91**, 155420 (2015).
[55] Y.-G. Yoon, P. Delaney, and S. G. Louie, Phys. Rev. B **66**, 073407 (2002).
[56] F. Triozon, S. Roche, A. Rubio, and D. Mayou, Phys. Rev. B **69**, 121410(R) (2004).
[57] S. Uryu and T. Ando, Phys. Rev. B **72**, 245403 (2005).
[58] J.-C. Charlier, X. Blase, and S. Roche, Rev. Mod. Phys. **79**, 677 (2007).
[59] S. Uryu and T. Ando, Phys. Rev. B **76**, 155434 (2007).
[60] M. Koshino, P.-K. Moon, and Y.-W. Son, Phys. Rev. B **91**, 035405 (2015).
[61] W. A. de Heer, C. Berger, X.-S. Wu, P. N. First, E. H. Conrad, X.-B. Li, T.-B. Li, M. Sprinkle, J. Hass, M. L. Sadowski, M. Potemski, and G. Martinez, Solid State Commun. **143**, 92 (2007).
[62] M. L. Sadowski, G. Martinez, M. Potemski, C. Berger, and W. A. de Heer, Phys. Rev. Lett. **97**, 266405 (2006).
[63] M. L. Sadowski, G. Martinez, M. Potemski, C. Berger, and W. A. de Heer, Solid State Commun. **143**, 123 (2007).
[64] X.-S. Wu, X.-B. Li, Z.-M. Song, C. Berger, and W. A. de Heer, Phys. Rev. Lett. **98**, 136801 (2007).
[65] J. Hass, R. Feng, J. E. Millan-Otoya, X. Li, M. Sprinkle, P. N. First, W. A. de Heer, E. H. Conrad, and C. Berger, Phys. Rev. B **75**, 214109 (2007).
[66] J. Hass, F. Varchon, J. E. Millan-Otoya, M. Sprinkle, N. Sharma, W. A. de Heer, C. Berger, P. N. First, L. Magaud, and E. H. Conrad, Phys. Rev. Lett. **100**, 125504 (2008).
[67] M. Sprinkle, D. Siegel, Y. Hu, J. Hicks, A. Tejeda, A. Taleb-Ibrahimi, P. Le Fevre, F. Bertran, S. Vizzini, H. Enriquez, S. Chiang, P. Soukiassian, C. Berger, W. A. de Heer, A. Lanzara, and E. H. Conrad, Phys. Rev. Lett. **103**, 226803 (2009).
[68] W. A. de Heer, C. Berger, X.-S. Wu, M. Sprinkle, Y. Hu, M. Ruan, J. A. Stroscio, P. N. First, R. Haddon, B. Piot, C. Faugeras, M. Potemski, and J.-S. Moon, J. Phys. D: Appl. Phys. **43**, 374007 (2010).
[69] W. A. de Heer, C. Berger, M. Ruan, M. Sprinkle, X.-B. Li, Y. Hu, B.-Q. Zhang, J. Hankinson, and E. Conrad, Proc. Natl. Acad. Sci. USA **108**, 16900 (2011).
[70] M. Orlita, C. Faugeras, P. Plochocka, P. Neugebauer, G. Martinez, D. K. Maude, A.-L. Barra, M. Sprinkle, C. Berger, W. A. de Heer, and M. Potemski, Phys. Rev. Lett. **101**, 267601 (2008).
[71] D. L. Miller, K. D. Kubista, G. M. Rutter, M. Ruan, W. A. de Heer, P. N. First, and J. A. Stroscio, Science **324**, 924 (2009).
[72] J. M. B. Lopes dos Santos, N. M. R. Peres, and A. H. Castro Neto, Phys. Rev. Lett. **99**, 256802 (2007).
[73] S. Latil, V. Meunier, and L. Henrard, Phys. Rev. B **76**, 201402 (2007).
[74] S. Shallcross, S. Sharma, and O. A. Pankratov, Phys. Rev. Lett. **101**, 056803 (2008).
[75] R. Bistritzer and A. H. MacDonald, Phys. Rev. B **84**, 035440 (2011).
[76] R. Bistritzer and A. H. MacDonald, Proc. Natl. Acad. Sci. USA **108**, 12233 (2011).
[77] J. M. B. Lopes dos Santos, N. M. R. Peres, and A. H. Castro Neto, Phys. Rev. B **86**, 155449 (2012).
[78] P.-K. Moon and M. Koshino, Phys. Rev. B **85**, 195458 (2012).
[79] P.-K. Moon and M. Koshino, Phys. Rev. B **87**, 205404 (2013).
[80] C.-K. Lu and H. A. Fertig, Phys. Rev. B **89**, 085408 (2014).
[81] E. J. Mele, Phys. Rev. B **81**, 161405 (2010).
[82] E. J. Mele, Phys. Rev. B **84**, 235439 (2011).
[83] Z.-H. Ni, Y.-Y. Wang, T. Yu, Y.-M. You, and Z.-X. Shen, Phys. Rev. B **77**, 235403 (2008).
[84] H. Schmidt, T. Lüdtke, P. Barthold, and R. J. Haug, Phys. Rev. B **81**, 121403 (2010).
[85] A. Luican, G.-H. Li, A. Reina, J. Kong, R. R. Nair, K. S. Novoselov, A. K. Geim, and E. Y. Andrei, Phys. Rev. Lett. **106**, 126802 (2011).
[86] I. Brihuega, P. Mallet, H. Gonzalez-Herrero, G. Trambly de Laissardiere, M. M. Ugeda, L. Magaud, J. M. Gomez-Rodriguez, F. Ynduraain, and J.-Y. Veuillen, Phys. Rev. Lett. **109**, 196802 (2012).
[87] G.-H. Li, A. Luican, J. M. B. Lopes dos Santos, A. H. Castro Neto, A. Reina, J. Kong, and E. Y. Andrei, Nat. Phys. **6**, 109 (2010).
[88] J. C. Slater and G. F. Koster, Phys. Rev. **94**, 1498 (1954).
[89] I. L. Spain, in *Chemistry and Physics of Carbon*, edited by P. L. Walker Jr. and P. A. Thrower (Marcel Dekker, New York, 1973), Vol. 8, p. 1.
[90] M. S. Dresselhaus, G. Dresselhaus, K. Sugihara, I. L. Spain, and H. A. Goldberg, *Graphite Fibers and Filaments*, Vol. 5 of Springer Series in Materials Science (Springer, Berlin, 1988).
[91] J. W. Mintmire and C. T. White, Carbon **33**, 893 (1995).
[92] T. Nakanishi and T. Ando, J. Phys. Soc. Jpn. **70**, 1647 (2001).
[93] S. Uryu, Phys. Rev. B **69**, 075402 (2004).
[94] T. Ando, J. Phys. Soc. Jpn. **69**, 1757 (2000).
[95] T. Ando, J. Phys. Soc. Jpn. **78**, 104703 (2009).
[96] S. M. Bachilo, M. S. Strano, C. Kittrell, R. H. Hauge, R. E. Smalley, and R. B. Weisman, Science **298**, 2361 (2002).
[97] M. J. O'Connell, S. M. Bachilo, C. B. Huffman, V. C. Moore, M. S. Strano, E. H. Haroz, K. L. Rialon, P. J. Boul, W. H. Noon, C. Kittrell, J. Ma, R. H. Hauge, R. B. Weisman, and R. E. Smalley, Science **297**, 593 (2002).
[98] R. B. Weisman and S. M. Bachilo, Nano Lett. **3**, 1235 (2003).
[99] Y. Shibuta and J. A. Elliott, Chem. Phys. Lett. **512**, 146 (2011).
[100] Y.-W. Son, S.-M. Choi, Y. P. Hong, S. Woo, and S.-H. Jhi, Phys. Rev. B **84**, 155410 (2011).
[101] Z. Liu, K. Suenaga, P. J. F. Harris, and S. Iijima, Phys. Rev. Lett. **102**, 015501 (2009).
[102] D. Zhan, L. Liu, Y. N. Xu, Z. H. Ni, J. X. Yan, C. Zhao, and Z. X. Shen, Sci. Rep. **1**, 12 (2011).